Check for updates

JGR Oceans

RESEARCH ARTICLE

10.1029/2024JC022313

Key Points:

- The atmospheric near-surface layer exhibits dominating stable and neutral conditions in the Arctic summer
- The contrast of years 2020 and 2022 shows correlation between stabilizing (destabilizing) effect and northward (southward) air advection
- Under stable conditions, the warmer skin layer can reduce bulk sea surface temperature-based turbulent heat flux estimates by about 9%

Correspondence to:

Y. Chen,
yanxu.chen@whoi.edu

Citation:

Chen, Y., Yu, L., & Zhang, C. (2025). Impacts of atmospheric near-surface stability on the Arctic summer air-sea heat budget using uncrewed surface vehicles. *Journal of Geophysical Research: Oceans*, *130*, e2024JC022313. https://doi.org/10.1029/2024JC022313

Received 31 DEC 2024
Accepted 17 JUN 2025

Author Contributions:

Conceptualization: Yanxu Chen, Lisan Yu
Data curation: Yanxu Chen
Formal analysis: Yanxu Chen
Funding acquisition: Lisan Yu, Chidong Zhang
Investigation: Yanxu Chen
Methodology: Yanxu Chen, Lisan Yu
Project administration: Lisan Yu, Chidong Zhang
Resources: Yanxu Chen, Chidong Zhang
Software: Yanxu Chen
Supervision: Lisan Yu, Chidong Zhang
Validation: Yanxu Chen
Visualization: Yanxu Chen
Writing – original draft: Yanxu Chen
Writing – review & editing: Yanxu Chen, Lisan Yu, Chidong Zhang

© 2025. American Geophysical Union. All Rights Reserved.

Impacts of Atmospheric Near-Surface Stability on the Arctic Summer Air-Sea Heat Budget Using Uncrewed Surface Vehicles

Yanxu Chen[1], Lisan Yu[1], and Chidong Zhang[2]

[1]Department of Physical Oceanography, Woods Hole Oceanographic Institution, Woods Hole, MA, USA, [2]Pacific Marine Environmental Laboratory, NOAA, Seattle, WA, USA

Abstract The atmospheric marine boundary layer (AMBL) plays a crucial role in regulating air-sea interactions and influencing the climate system, particularly in the Arctic due to its high sensitivity to global warming. This study utilizes five years (2018–2022) of saildrone data from the Bering-Chukchi-Beaufort Seas to analyze atmospheric near-surface stability and air-sea turbulent heat fluxes during the Arctic summer. By applying Monin-Obukhov similarity theory, we investigate the temporal variability and mechanisms that influence AMBL stability. Our findings reveal two distinct regimes of stable and unstable conditions in two contrasting years of 2020 and 2022. In 2020, cold air advection driven by northerly winds consistently destabilizes the AMBL, leading to increased oceanic heat loss. In 2022, however, southerly winds and warm air advection stabilize the AMBL, suppressing air-sea heat exchanges. The temporal variation of turbulent heat fluxes is primarily driven by air-sea temperature differences, with the magnitude of wind speed and its temperature covariance serving as secondary factors. We also show the importance of skin temperature measurements from saildrones for improving estimates of turbulent heat fluxes. These insights enhance our understanding of Arctic air-sea interactions and inform climate models, underscoring the need for high-resolution observations in polar regions and the improvement of bulk flux parameterization for stable AMBL.

Plain Language Summary This study investigates how the Arctic summer atmosphere, specifically the atmospheric marine boundary layer (AMBL), interacts with the ocean and how it transitions from summer to autumn. The AMBL is a thin layer of air above the sea, playing a crucial role in weather and climate by affecting heat and moisture exchange. To better understand this interaction, researchers have developed an innovative tool called the "saildrone"—an uncrewed, wind-powered boat that makes measurements within the AMBL. In this study, we use saildrone data from 2018 to 2022 to investigate variations in air-sea heat exchange, particularly focusing on how this exchange varies under different weather conditions. Our findings show that accurate measurements of sea surface temperature are essential for understanding these interactions. Traditional methods that only measure the water temperature a few meters below the surface may not fully capture the heat exchange process and can overestimate its magnitude. By using the saildrone's measurement of skin temperature, which is the one that directly communicates with the atmosphere, we can improve estimates of how much heat is exchanged at the air-sea interface.

1. Introduction

The atmospheric marine boundary layer (AMBL) is a critical interface where the atmosphere interacts with the ocean, profoundly influencing global climate dynamics. This layer, typically extending from the ocean surface to a few hundred meters, plays a pivotal role in regulating the exchange of momentum, heat, and moisture between the ocean and atmosphere. Due to interests in air-sea interaction, the definition of AMBL in this study is limited to the near-surface layer. Central to understanding these interactions is the concept of Monin-Obukhov similarity theory (hereafter MOST) (Monin & Obukhov, 1954), which characterizes the vertical turbulent structures and gradients within the AMBL and has been widely used in numerical weather predictions (Grachev & Fairall, 1997). According to MOST, for a distance from the ground z, the nondimensional turbulence statistics are determined by a dimensionless parameter $\zeta = z/L$, where L is the Monin-Obukhov length, the absolute value of which represents the height at which the buoyancy and shear production rates of turbulent kinetic energy are of the same order.

The MOST parameter ζ has been widely used to determine the stability of the AMBL. In stable conditions, cooler sea surfaces promote air stratification, suppressing turbulent mixing and reducing the efficiency of heat and gas exchanges (Berström & Smedman, 1995; Brooks et al., 2003). This suppression of vertical mixing can cause pollutants and moisture to accumulate near the surface, leading to the development of stratus or stratocumulus clouds and haze or fog (Betts & Boers, 1990). Reduced wind-induced turbulence results in a relatively smooth sea surface. Conversely, in unstable conditions driven by warmer sea surface temperatures, turbulence intensifies, enhancing mixing and potentially stimulating cumulus cloud formation and increasing precipitation (Atlas et al., 1986). Enhanced mixing and increased wind help disperse pollutants and moisture, leading to better visibility and rougher sea conditions. Under moderate to strong winds, an inclusion of wind-wave correction to stability may lead to higher surface stress and momentum flux into the ocean (Sauvage et al., 2023). Neutral conditions of stability have also been defined based on various empirical experiments and locations (Sorbjan & Grachev, 2010).

The bulk flux algorithms are universally constructed based on theories of stability (Bonino et al., 2022; Cronin et al., 2019; Fairall et al., 2003; Kara et al., 2000; Kondo, 1975; McPhaden & Hayes, 1991; Yu, 2019). In these algorithms, the air-sea interfacial turbulent fluxes of momentum and heat are represented in terms of the bulk meteorological variables through empirical transfer coefficients (often referred to as drag coefficients), which are analytically determined by ζ. An analogy of the ocean surface layer to the AMBL has also been created and applied as upper-ocean mixing schemes known as the K-profile parameterization (Large et al., 1994; Roekel et al., 2018; Zheng et al., 2021). Second-order mechanisms modifying AMBL stability have also been studied through, for example, (a) the prevalence of spatial roughness (or temperature) gradients, specifically termed as internal stable layers in coastal regions (Ma & Mahesh, 2023; Rogers et al., 1995; Smedman et al., 1997), and (b) thermal feedback to wind stress in the context of air-sea coupling processes of the open ocean, where the crosswind sea surface temperature (SST) gradient is associated with wind vorticity while downwind SST gradient is linked to wind divergence (Chelton & Xie, 2010; Renault et al., 2023).

In this study, we utilize MOST to investigate the air-sea heat budget during the Arctic summer. Recent observations indicate that the Arctic is warming at nearly twice the global average rate, a phenomenon known as Arctic amplification (Serreze & Barry, 2011). This accelerated warming leads to substantial reductions in sea ice extent, resulting in increased areas of open water during the summer months. These changes profoundly affect the AMBL's structure and dynamics influencing cloud formation, atmospheric stability, and surface energy budgets (Seo & Yang, 2013; Uttal et al., 2002). In addition, it has been found that a predominant temperature inversion in the lower troposphere exists in all seasons, referred to as the Arctic inversion (Tjernström et al., 2012; Tjernström & Graversen, 2009). The Arctic vertical structure is influenced by many factors, such as warm air advection, sea ice melting that alters the albedo, cloud-top cooling, and turbulent mixing (Vihma, 2014). In addition, the frequency and intensity of Arctic storms are projected to increase with continued climate warming and sea ice retreat, contributing to enhanced surface fluxes and vertical mixing in the AMBL (Cohen et al., 2024). Thus, the investigations of the AMBL structure evolution and its controlling factors are key to understanding the Arctic warming feedback.

Due to a lack of observations, there have been few analyses of the Arctic AMBL based on in situ data. The Arctic AMBL was studied several decades ago during the Surface Heat Budget of the Arctic Ocean (SHEBA) campaign (Andreas et al., 2002; Persson et al., 2002; Uttal et al., 2002). More recent research is based on the Multidisciplinary Drifting Observatory for the Study of Arctic Climate (MOSAiC) campaign, a year-long icebreaker expedition conducted from September 2019 to October 2020 (Jozef et al., 2024). Regarding the Arctic air-sea heat budget, the SHEBA study by Andreas et al. (2002) shows that relative humidity measured in open leads and polynyas is consistently near 100% (saturation with respect to ice). This near-saturation or sometimes supersaturation is attributed to the rapid supply of water vapor from these open water areas, outpacing any removal by sea ice surfaces or synoptic processes. The MOSAiC study by Peng et al. (2023) demonstrates that warm air advection predominantly drives temperature inversions during the Arctic summer with surface temperatures constrained by sea ice melting. Their research also indicates a more suppressed AMBL height during the MOSAiC campaign compared to the SHEBA campaign, highlighting significant variability in the Arctic AMBL structure during the summer melting season. Although these studies have improved our understanding of the thermal features in the near-surface layer of the Arctic Ocean, their impact on air-sea heat fluxes remains unclear.

21699291, 2025, 7, Downloaded from https://agupubs.onlinelibrary.wiley.com/doi/10.1029/2024JC022313 by Mbl Whoi Library, Wiley Online Library on [30/06/2025]. See the Terms and Conditions (https://onlinelibrary.wiley.com/terms-and-conditions) on Wiley Online Library for rules of use; OA articles are governed by the applicable Creative Commons License

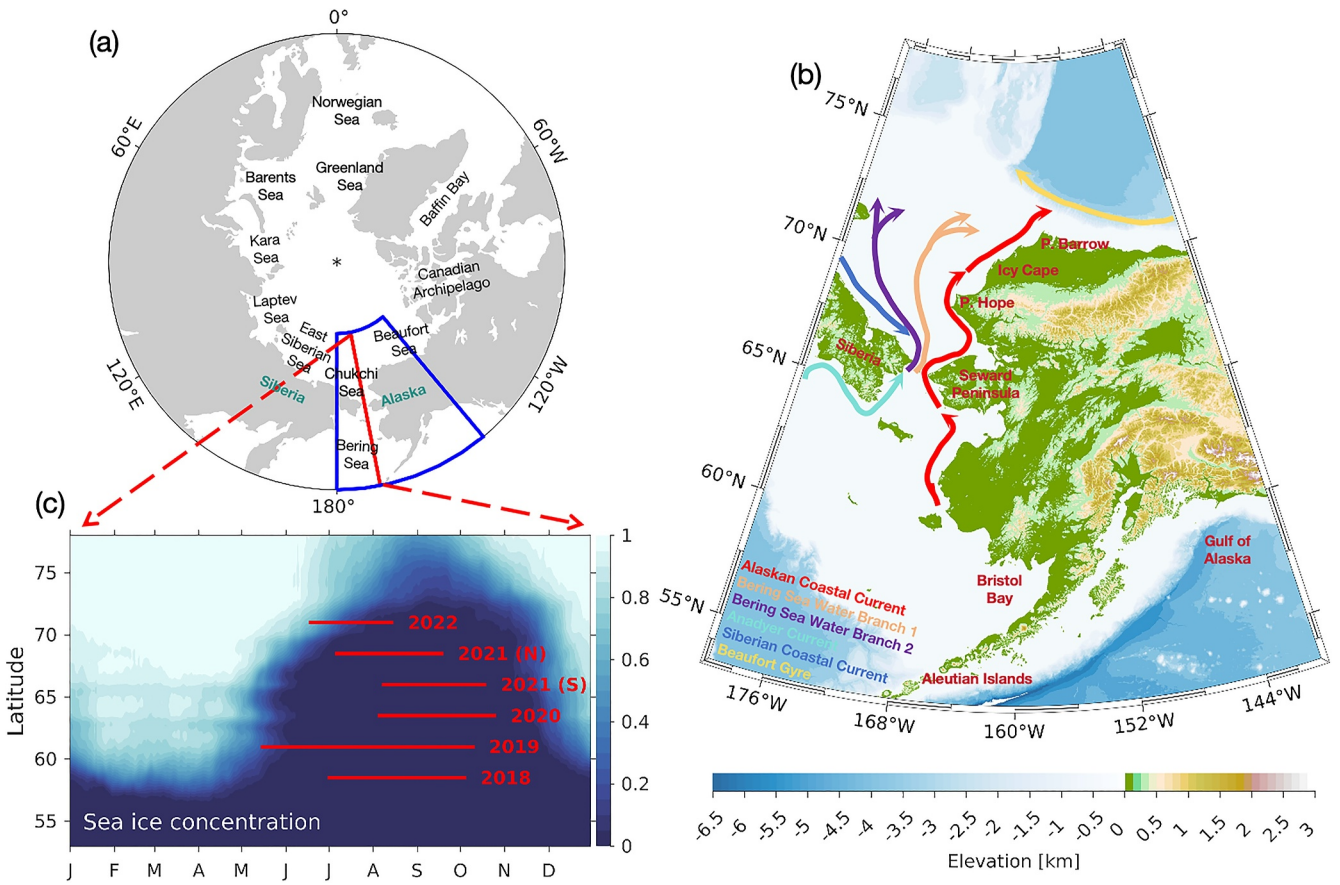

Figure 1. Study region of the Bering, Chukchi, and Beaufort Seas. (a) General geographical map. (b) Ocean surface currents and topography within the study area. (c) Time span of saildrone measurements over 5 years, superimposed on annual sea ice concentration variability as a function of latitude.

To enhance our understanding of AMBL characteristics and the surface energy budget under changing Arctic conditions, more comprehensive observations are required. The Arctic saildrone deployment aims to address this need. Saildrones are uncrewed surface vehicles (USVs) designed to access remote and harsh Arctic environments to gather crucial atmospheric and oceanic data. These innovative platforms use wind for propulsion and solar energy to power sensors, vehicle control, onboard real-time data processing, and transmission to enable a long travel endurance. Saildrones complement and support the limited crewed research cruises in the Arctic, significantly increasing domain awareness and improving the collection of critical data in a rapidly evolving environment. In addition to the commonly used SST measurements a few meters below the surface, saildrones deployed by NASA teams also measure skin SST using radiometers. This capability is valuable for validating AMBL stability based on MOST and assessing the accuracy of air-sea turbulent heat flux (THF) algorithms based on inferred stability. Although this study does not use the eddy covariance method, prior evaluations have demonstrated the consistency between eddy covariance and bulk fluxes derived from saildrone observations, supporting the validity of the bulk approach employed here (Edson et al., 1998; Reeves Eyre et al., 2023).

This study aims to investigate the characteristics and dynamics of the air-sea heat fluxes for the Bering-Chukchi-Beaufort Seas, with a focus on the impact of synoptic-scale events and resulting changes in stability conditions and how they affect the near-surface heat budgets. By analyzing observational data and employing MOST, we aim to elucidate the mechanisms driving modifications in AMBL stability, providing critical insights into the evolving climate system of the Arctic. Figure 1 below illustrates: (a) the study region encompassing the Bering-Chukchi-Beaufort Seas, (b) the topography and ocean current systems, and (c) the temporal span of all saildrone measurements conducted over five consecutive years from 2018 to 2022. Sea ice concentration in (c) indicates that coverage extends to as far south as 55°N in winter and retreats rapidly between June and October reaching as far north as 75°N. Global warming has led to increasingly vast ice-free areas opening up each year, facilitating

21699291, 2025, 7, Downloaded from https://agupubs.onlinelibrary.wiley.com/doi/10.1029/2024JC022313 by Mbl Whoi Library, Wiley Online Library on [30/06/2025]. See the Terms and Conditions (https://onlinelibrary.wiley.com/terms-and-conditions) on Wiley Online Library for rules of use; OA articles are governed by the applicable Creative Commons License

more vigorous air-sea interactions. This situation underscores the need for a resilient ocean observing platform capable of adapting to rapidly changing sea ice conditions. In addition, the absence of sea ice during the Arctic summer has been shown to favor stable conditions in the AMBL due to enhanced surface heating and moisture fluxes (Persson, 2012; Tjernström et al., 2012). Furthermore, surface ocean currents, such as the inflow of warm Pacific water through the Bering Strait, may influence the regional freshwater budget and precondition the summer air-sea heat exchange by modifying upper-ocean stratification (Proshutinsky et al., 2009; Woodgate, 2018).

In the next section, we begin with the overview of data used to measure the sea surface heat budget of the Arctic summer, continue with a description of the definitions of AMBL stability and end with the commonly used method of THF calculation. The results are presented in three subsections: (a) a description of Arctic summer air-sea heat flux characteristics, (b) a comparison of two scenarios that lead to stable and unstable AMBL conditions, and (c) a discussion on how AMBL stability affects the air-sea heat budget during the Arctic summer. Finally, we provide a summary and discuss the study's limitations as well as potential directions for future research.

2. Data and Methods

2.1. Arctic Surface Layer Measurements From USVs

The development of saildrones into a scientific air-sea interaction observing platform started in 2014 between Saildrone Inc. and the NOAA Pacific Marine Environmental Laboratory (PMEL) (Meinig et al., 2019). A saildrone has a 7-m long hull, a rigid wing of about 5 m above the water line and a keel at the depth of 2.5 m. Batteries and solar panels power the onboard navigational electronics, which include automated identification system transceivers and Global Positioning System navigational systems, as well as scientific instrumentation and satellite telemetry of data and navigational instructions. Several studies from NOAA PMEL and NASA also detail the configuration of saildrones (e.g., Figure 1 in Zhang et al. (2019)), so that information is not repeated here.

The saildrone measurements used in this study were part of a collaboration between Saildrone Inc., NOAA PMEL and NASA's National Oceanographic Partnership Program, as summarized in Table 1. Each saildrone was equipped with: (a) a Rototronic HC2-S3 sensor at 2.3 m height to measure air temperature and relative humidity, (b) a Sea-Bird SBE37 Microcat at 0.5 m depth to measure seawater conductivity and temperature, which together provide seawater salinity, (c) a Vaisala PTB210 Barometer on the hull (0.2 m height) to measure sea level pressure, and (d) a Gill model 1590-PK-020 anemometer atop the wing (5.2 m height) to provide three-dimensional wind velocity at 10 Hz. The higher frequency data were stored onboard for access upon vehicle recovery.

Figure 2 displays the saildrone tracks over the 5 years, along with the June-to-September averaged map of ERA5 sea level pressure and wind direction at the sea surface (Hersbach et al., 2020). The wind roses illustrate the predominant wind direction at the specific location of 169°W, 70°N. Across all five years, the primary wind direction at this location is northeasterly with 2020 showing this trend most strongly. Moreover, the maximal wind speed at this location is no more than 10–15 m s^{-1} during these 4 months in the Arctic summer.

For all 5 years, a cyclonic wind pattern is observed across the Bering Strait, characterized by low sea level pressure at the center where the air rises vertically. As the air rises and cools, water vapor condenses to form clouds and potentially precipitation. Such is the 4-month averaged picture of the near-surface meteorology in Figure 2. However, with the help of saildrones, our study analyzes cases where wind direction controls the AMBL stability and differs from this picture of a long-term mean. Specifically, under stable to neutral conditions, the saturated air in the Arctic summer does not lead to precipitation (Andreas et al., 2002).

Together, Table 1 and Figure 2 summarize the locations and time ranges of the saildrone measurements over 5 years, along with temporally averaged maps that illustrate general meteorological patterns. More details on each saildrone's measurement will be provided in the results section. In 2018, four saildrones were launched from Dutch Harbor, AK, on June 30th to sail north through the Bering Strait and the Chukchi Sea into the Arctic Ocean. These saildrones undertook two concurrent 3-month missions to measure carbon dioxide and the abundance of Arctic cod. The data collected aimed to identify ongoing changes in the Arctic ecosystem and how these changes might impact the food web and large-scale climate and weather systems. For the 2019 Arctic Saildrone Mission, five of six vehicles (SD1033, SD1034, SD1035, SD1036, and SD1037) sailed into the Chukchi Sea, whereas the sixth vehicle (SD1041) remained in the Bering Sea primarily to measure fish acoustic backscatter.

21699291, 2025, 7, Downloaded from https://agupubs.onlinelibrary.wiley.com/doi/10.1029/2024JC022313 by Mbl Whoi Library, Wiley Online Library on [30/06/2025]. See the Terms and Conditions (https://onlinelibrary.wiley.com/terms-and-conditions) on Wiley Online Library for rules of use; OA articles are governed by the applicable Creative Commons License

Table 1
Summary of All Saildrones Used in This Study

Year	Name	Month range	Latitude range (°N)	High-accuracy skin temperature?	Source
2018	SD1020	July–October	53.8–72.3	N	NOAA
	SD1021	July–October	53.8–73.0	N	NOAA
	SD1022	July–October	53.8–71.5	N	NOAA
	SD1023	July–October	53.8–72.5	N	NOAA
2019	SD1033	May–October	53.8–73.1	N	NOAA
	SD1034	May–October	53.8–75.4	N	NOAA
	SD1035	May–September	53.8–75.3	N	NOAA
	SD1036	May–October	53.8–75.2	Y	NASA
	SD1037	May–October	53.9–75.5	Y	NASA
	SD1041	May–October	53.8–65.3	N	NOAA
2020	SD1037	August–October	57.8–72.8	N	NOAA
	SD1055	August–September	68.3–72.4	N	NOAA
	SD1068	August–October	57.7–72.3	N	NOAA
	SD1069	August–October	55.2–69.9	N	NOAA
2021	SD1030	August–October	56.9–64.2	N	NOAA
	SD1033	August–October	53.9–64.1	N	NOAA
	SD1034	August–October	53.9–64.2	N	NOAA
	SD1067	August–October	54.0–64.1	N	NOAA
	SD1057	July–September	65.2–70.9	Y	NASA
	SD1058	July–September	65.2–70.9	Y	NASA
2022	SD1041	June–August	65.2–68.3	N	NASA
	SD1046	June–August	65.3–71.6	N	NASA

Note. NASA-deployed saildrones are equipped with infrared radiometers that provide high-quality measurements of sea surface skin temperature, enabling improved validation and analysis of air-sea heat fluxes.

In 2020, four saildrones sailed from San Francisco to the Chukchi Sea for the Arctic Mapping Mission, which aimed to address significant gaps in providing modern, accurate mapping data of the Bering Sea and Alaska's North Slope. In 2021, four NOAA saildrones (SD1030, SD1033, SD1034, and SD1067) continued the investigation of bathymetric mapping south of the Bering Strait. Additionally, the 2021 NASA Saildrone Arctic campaign featured two saildrones (SD1057 and SD1058) deployed during a 76-day cruise in the Bering and Chukchi Seas. The primary objective for these NASA saildrones was to gather comprehensive atmospheric and oceanographic data in Alaskan Arctic waters with a focus on understanding the spatial and temporal scales of air-sea covariance in the Chukchi Sea. Similar deployments were also conducted in 2022.

2.2. Special Capabilities of NASA Saildrones: Skin Temperature Measurements

Table 1 shows that four NASA saildrones are equipped to measure high-accuracy sea surface skin temperatures: two in 2019 and two in 2021. This capability is achieved by installing two Heitronics infrared (IR) pyrometers on the foredeck at a height of 0.8 m above the waterline. These pyrometers operate in the wavelength range of 8–14 μm with one directed at the sea surface and the other at the sky. Sky radiance measurements are used to correct the sea-viewing IR spectral radiation data for the downward atmospheric radiance reflected at the sea surface (Jia et al., 2023).

In addition, all saildrones are equipped with SST instruments, including two CTD devices that measure seawater temperature at approximately 0.5 m depth. One CTD is an SBE 37-SMP-ODO pumped MicroCAT, and the other is an RBRconcerto 3. Both instruments provide accurate temperature measurements at depth. When possible, we use the averaged values from these two instruments for in-depth SST calculations.

21699291, 2025, 7, Downloaded from https://agupubs.onlinelibrary.wiley.com/doi/10.1029/2024JC022313 by Mbl Whoi Library, Wiley Online Library on [30/06/2025]. See the Terms and Conditions (https://onlinelibrary.wiley.com/terms-and-conditions) on Wiley Online Library for rules of use; OA articles are governed by the applicable Creative Commons License

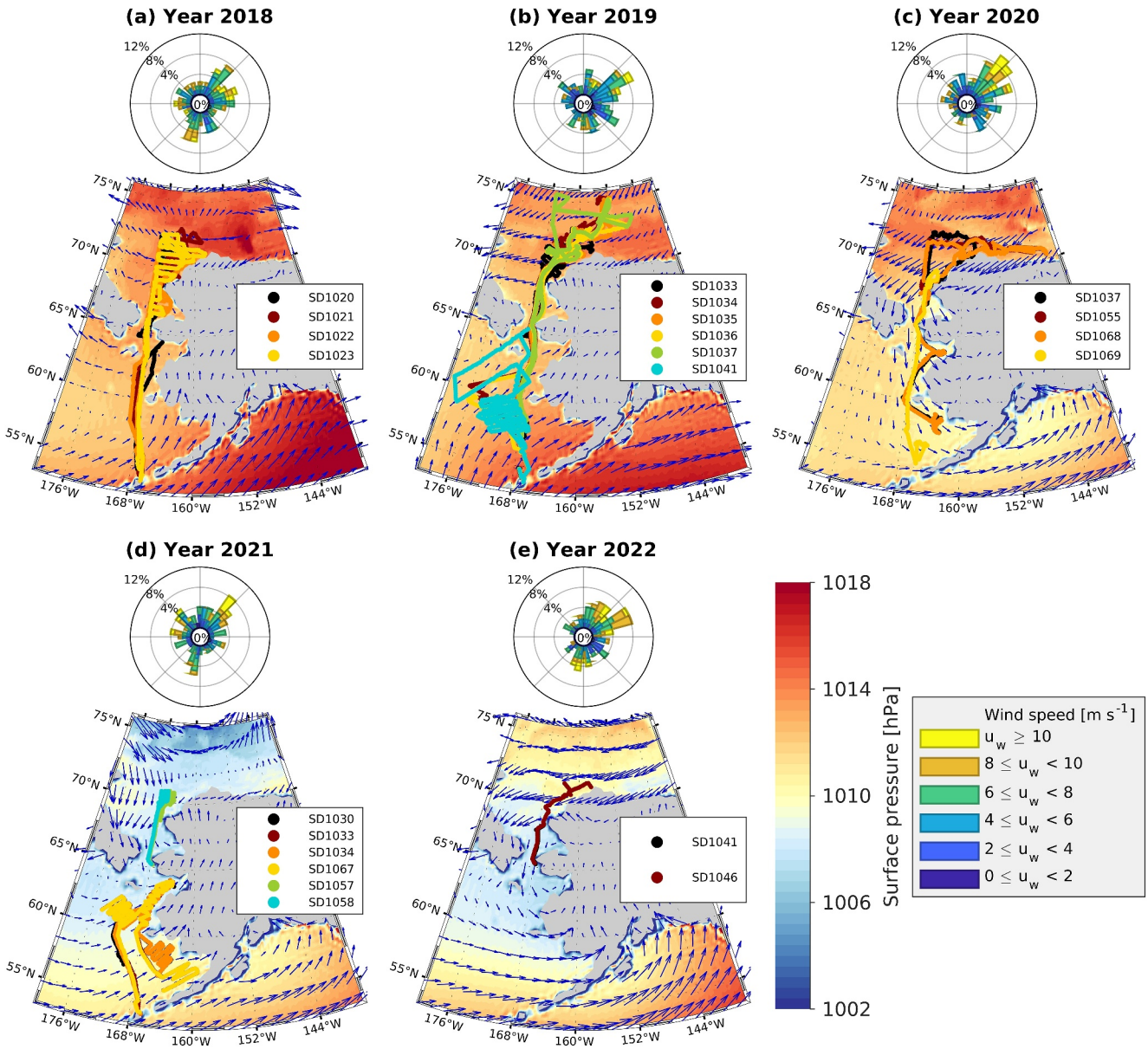

Figure 2. Saildrone locations in the Bering, Chukchi, and Beaufort Seas over five consecutive years (2018–2022). Background colors represent the ERA5 seasonal mean sea level pressure and 10-m wind field for June to September (Hersbach et al., 2020). The wind rose in each panel displays ERA5 wind vectors for a specific location of 169°W, 70°N. The ERA5 hourly wind patterns closely match those measured by the saildrones.

In this study, we compare the difference between in-depth SST and sea skin temperature using these four NASA saildrones and analyze how this difference influences the estimate of turbulent heat fluxes under various AMBL stability conditions. Unlike the typically observed cool skin effect (Saunders, 1967), where skin temperature is several tenths of a Kelvin lower than in-depth ocean temperature, our study investigates the warm layer effect during the Arctic summer (Section 3.3). The cool skin effect, occurring both day and night due to the skin layer's loss of energy through longwave emission, is influenced by interface temperature differences and shear-driven mixing. Literature often links the skin-bulk temperature difference to wind speed (note that in-depth SST is also referred to as bulk SST in our study). For example,

$$\Delta T = a + b \cdot \exp\left(-\frac{U}{c}\right), \tag{1}$$

21699291, 2025, 7, Downloaded from https://agupubs.onlinelibrary.wiley.com/doi/10.1029/2024JC022313 by Mbl Whoi Library, Wiley Online Library on [30/06/2025]. See the Terms and Conditions (https://onlinelibrary.wiley.com/terms-and-conditions) on Wiley Online Library for rules of use; OA articles are governed by the applicable Creative Commons License

where ΔT represents the difference between skin and in-depth temperatures, and U represents wind speed (typically measured at or adjusted to 10 m). The coefficients (a, b, and c) are often determined empirically (see Table 1 of Luo et al. (2022) for a range of cool skin physical models).

In contrast, the warm layer effect is recognized as a result of solar absorption during the daytime and can reach magnitudes of several Kelvins (Donlon et al., 2002; Fairall et al., 1996). Given the context of the cool skin effect with diurnal warming as a secondary effect, Jia et al. (2023) and Jia and Minnett (2023) recently developed a new empirical cool skin model incorporating diurnal warming in high-latitude environments, using data from the two NASA saildrones deployed in 2019. We also observe the cool skin effect using the 2019 saildrones; however, the additional data from 2021 provide further insights into the warm layer effect, which will be discussed in Section 3.3.

2.3. Definition of Stability for AMBL

We follow the similarity theory developed by Monin and Obukhov (Monin & Obukhov, 1954) (MOST) to delineate the vertical structure of an idealized atmospheric surface layer. The hypothesis is that under horizontally homogeneous and stationary conditions, every dimensionless scaling relationship in the surface layer is a universal function of the dimensionless parameter $\zeta = z/L$, the ratio of height z to the Obukhov length (Obukhov, 1971)

$$L = \frac{u_*^3}{\kappa B_0}, \tag{2}$$

where u_* is the friction velocity, $\kappa = 0.4$ is the von Karman constant, and $B_0 = -\overline{w'b'}|_0$ is the near-surface buoyancy flux. For the atmosphere, this buoyancy flux can be represented by the virtual potential temperature θ_v. Thus, the Obukhov length can also be expressed as

$$L = -\frac{u_*^3}{\kappa \frac{g}{\overline{\theta_v}} \overline{w'\theta_v'}|_0}. \tag{3}$$

When $L < 0$, the surface layer is statically unstable, and when $L > 0$ the surface layer is statically stable. The absolute magnitude of L indicates the deviation from statically neutral state, with smaller $|L|$ values corresponding to larger deviations from neutral conditions. When $|L|$ is small and $L < 0$, buoyant processes dominate the production of turbulent kinetic energy compared with shear production. By definition, under neutral conditions $L \to \infty$. It is obvious that L is equivalent to Richardson's criterion for dynamic stability and its magnitude is a rough estimate of the distance at which buoyancy production becomes dynamically important in the turbulent kinetic energy budget relative to surface shear production. Thus, L is used for nondimensionalization of height z in the similarity theory.

2.4. Air-Sea Turbulent Heat Flux and Its Variations

The MOST has been generally successful in describing the flux-profile relationships in the AMBL over a moderate range of z. It also laid a solid foundation for the establishment of bulk transfer relations (e.g., the COARE algorithm used in this study), since its formulation implicitly suggests a parameterization for turbulent heat fluxes in other locations without enough measurements of fluctuations. The traditional bulk flux algorithm COARE version 3.5 (Edson et al., 2013; Fairall et al., 1997, 2003) was utilized to calculate air-sea THF based on saildrone-borne state variables. The computation of latent heat (Q_{LH}) and sensible heat (Q_{SH}) fluxes is governed by the following formulas:

$$\begin{aligned} Q_{LH} &= \rho L_e c_e U(q_s - q_a), \\ Q_{SH} &= \rho c_p c_h U(T_s - T_a), \end{aligned} \tag{4}$$

where ρ represents air density and L_e denotes the latent heat of vapourization, which is a linear function of SST (T_s in the equation). The term c_p signifies the specific heat capacity of air at constant pressure. The coefficients c_e

21699291, 2025, 7, Downloaded from https://agupubs.onlinelibrary.wiley.com/doi/10.1029/2024JC022313 by Mbl Whoi Library, Wiley Online Library on [30/06/2025]. See the Terms and Conditions (https://onlinelibrary.wiley.com/terms-and-conditions) on Wiley Online Library for rules of use; OA articles are governed by the applicable Creative Commons License

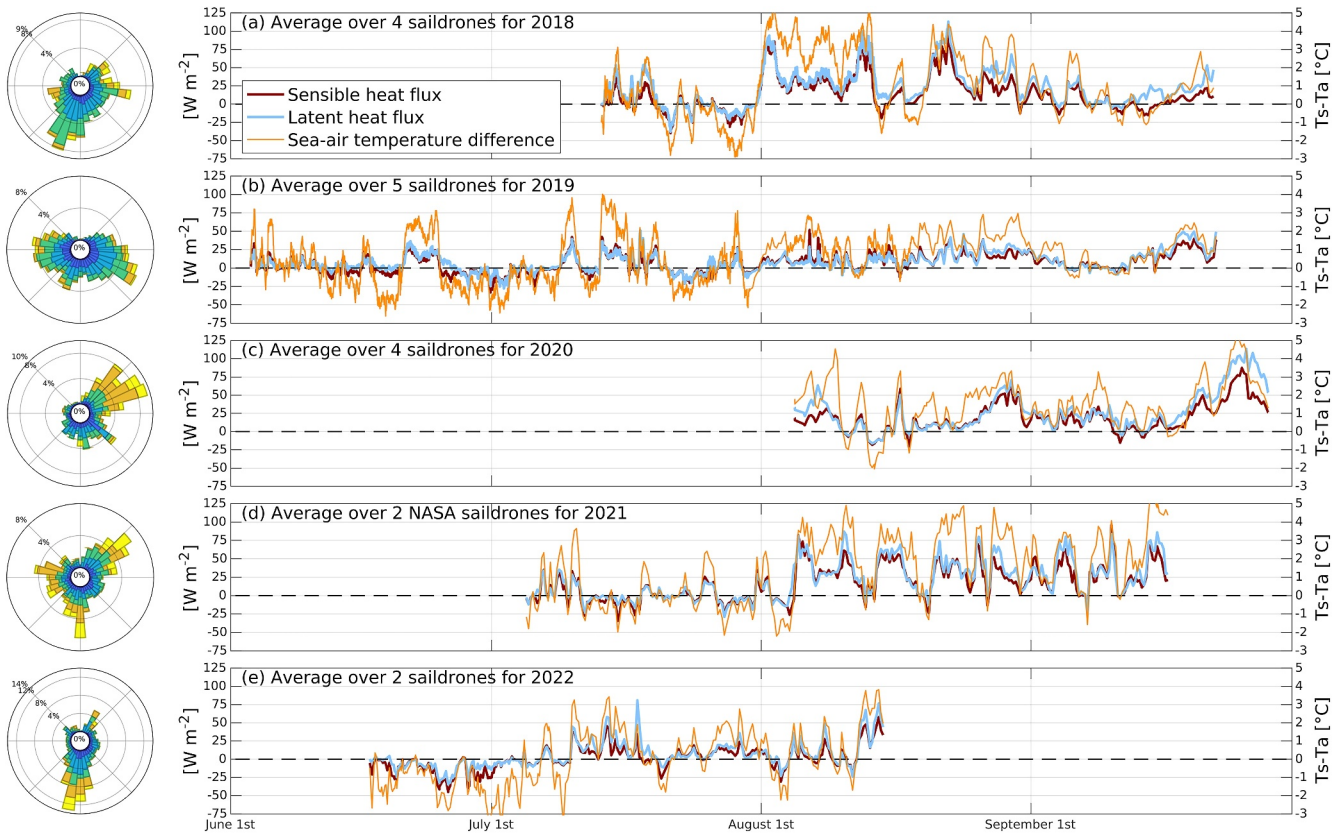

Figure 3. Time series of sensible heat fluxes, latent heat fluxes, and sea-air temperature differences from June to September (5 years from 2018 to 2022) measured by saildrones. Note that the latitudes are limited to higher than 65°N inside the Arctic circle. The wind rose associated with each panel shows the wind direction (from) measured at latitudes higher than 65°N. The number of saildrones used to construct the averaged time series for each year is indicated in each panel and also listed in Table 1.

and c_h are the stability- and height-dependent turbulent exchange coefficients for latent and sensible heat, respectively. The variables T_a and q_a represent the air temperature and specific humidity at a reference height of 2 m above the sea surface, and U indicates the wind speed at a reference height of around 5 m. The term q_s stands for the saturation humidity at T_s. These bulk formulas establish the relationship between Q_{LH} (Q_{SH}) and air-sea humidity difference (temperature difference) and wind speed.

In this study, we also analyze contributions from each covariance term to the total THF variation. Studies have found that changes in air temperature were more pronounced to THF variations than changes in wind speed during cold air advections in the Arctic summer (Carrigg et al., 2024).

To assess the individual impacts on the changes in Q_{SH} and Q_{LH}, these terms were decomposed into mean and anomalous components and reformulated as follows (Yu et al., 2023):

$$\begin{aligned} Q'_{LH} &= \rho L_e c_e\left(\bar{U}\Delta q' + U'\Delta\bar{q} + U'\Delta q'\right), \\ Q'_{SH} &= \rho c_p c_h\left(\bar{U}\Delta T' + U'\Delta\bar{T} + U'\Delta T'\right), \end{aligned} \tag{5}$$

where the overbars denote the time mean value over the entire observation period for each year and primes are deviations from the mean. If the effect of c_e and c_h is not considered, the three terms inside the brackets can be represented as follows: Qterm for $\bar{U}\Delta q'$, Tterm for $\bar{U}\Delta T'$, Wterm for $U'\Delta\bar{q}$ and $U'\Delta\bar{T}$, and Cterm for $U'\Delta q'$ and $U'\Delta T'$. These terms correspond to the contributions of moist, thermal, wind, and nonlinear covariance effects to the total variability. Time series of these terms and their relative contribution in percentage are shown in Figures 4 and 5.

21699291, 2025, 7, Downloaded from https://agupubs.onlinelibrary.wiley.com/doi/10.1029/2024JC022313 by Mbl Whoi Library, Wiley Online Library on [30/06/2025]. See the Terms and Conditions (https://onlinelibrary.wiley.com/terms-and-conditions) on Wiley Online Library for rules of use; OA articles are governed by the applicable Creative Commons License

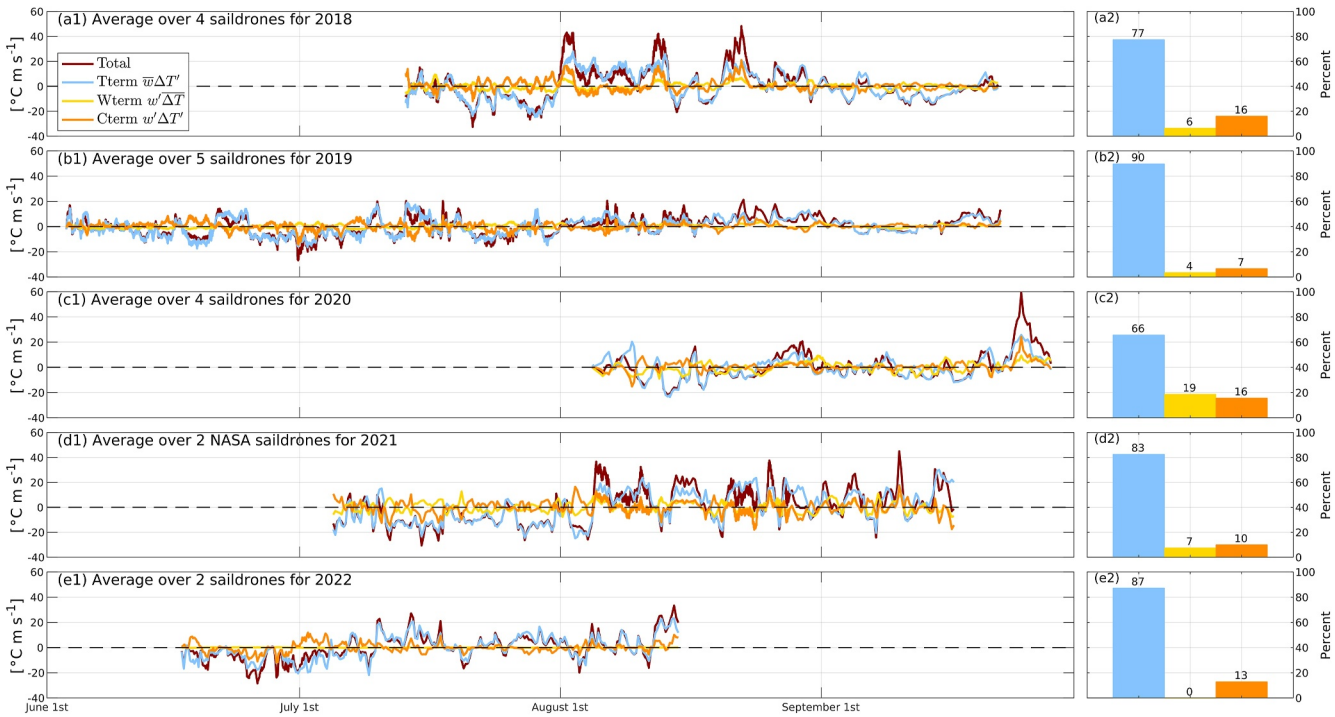

Figure 4. Covariance decomposition of sensible heat flux variation into three subterms for each year. The right panels show the percentage contribution of each subterm to the total sensible heat flux variation. The units of time series represent the product of temperature and wind speed.

2.5. Air-Sea Net Heat Flux

The net surface longwave and shortwave radiation data were retrieved from the Clouds and the Earth's Radiant Energy System (CERES) SYN1deg product (Doelling et al., 2016). The net air-sea heat flux is computed by summing the radiative and turbulent heat fluxes as follows:

$$Q_{NET} = Q_{SW} + Q_{LW} + Q_{SH} + Q_{LH}. \tag{6}$$

The spatial resolution of CERES radiation data is $1° \times 1°$, whereas each saildrone measurement has a temporal interval of approximately 60 s, although not all time steps include measurements of humidity, temperature, and wind. With an average sailing speed of about 3 knots (dependent on wind conditions), the spatial resolution of the saildrone measurements is approximately 50 m. Therefore, we use these high-resolution measurements to perform frequency and wavenumber analyses of air-sea heat fluxes across the Bering Strait. For the purposes of this study, all fluxes are defined as positive when directed upward and negative when directed downward. Positive values indicate the addition of heat to the atmosphere (resulting in a cooling effect for the ocean), whereas negative values signify the surplus of heat to the ocean (resulting in a warming effect).

3. Results

3.1. Air-Sea Heat Fluxes in the Arctic Summer

The evolution of sensible heat flux, latent heat flux, and sea-air temperature differences for the summer periods over five consecutive years is illustrated in Figure 3. Each year's wind rose diagram highlights the highly variable nature of near-surface wind directions. For the meridional components, the predominant southerly winds in 2018, 2019, and 2022 brought warm air from lower latitudes. In contrast, 2020 saw cold air advection from the northeastern region, whereas 2021 experienced more variable wind patterns with competing southerlies and northeasterlies. These wind roses differ from those in Figure 2, which represents the entire June to September season and highlights predominant cold advection from the northeast. In terms of the relative location between land and ocean, eastward wind directions are frequently observed south of the Bering Strait, whereas westward wind directions are more pronounced north of it (as shown in Figure 2). Additionally, Figure 3 shows that at

21699291, 2025, 7, Downloaded from https://agupubs.onlinelibrary.wiley.com/doi/10.1029/2024JC022313 by Mbl Whoi Library, Wiley Online Library on [30/06/2025]. See the Terms and Conditions (https://onlinelibrary.wiley.com/terms-and-conditions) on Wiley Online Library for rules of use; OA articles are governed by the applicable Creative Commons License

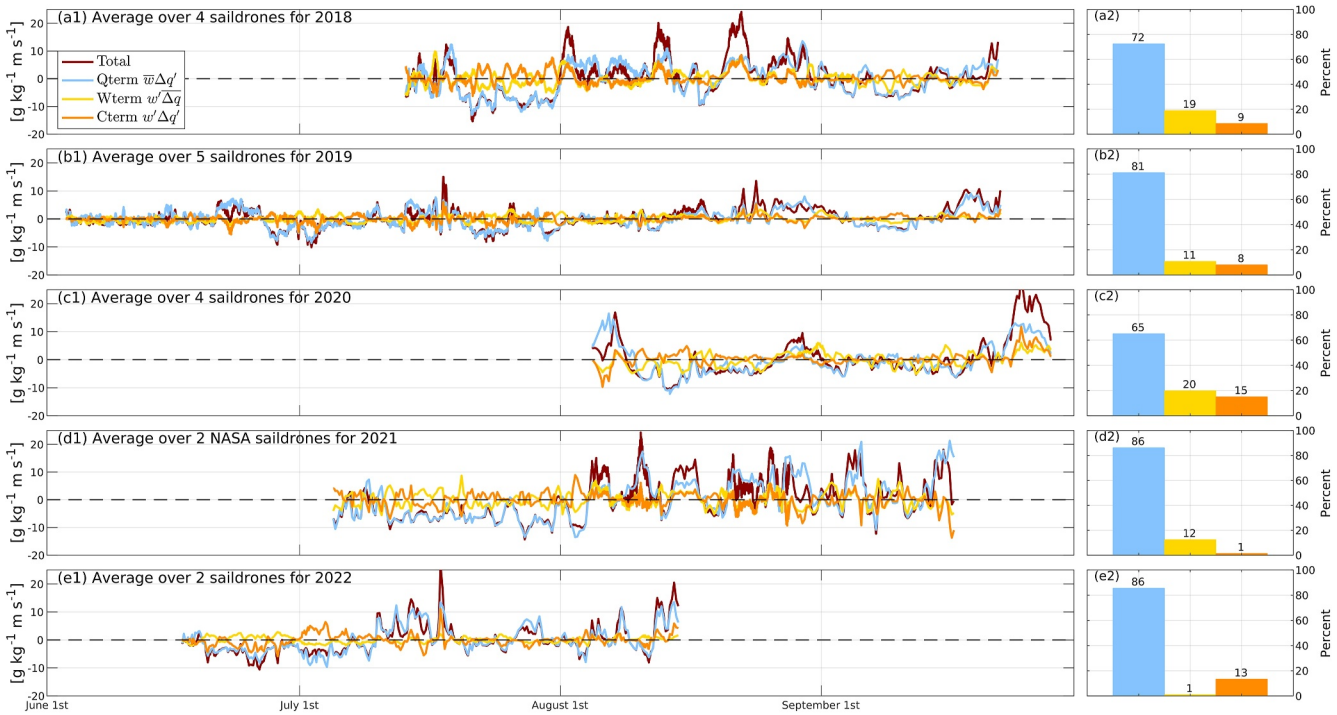

Figure 5. Same as Figure 4 but for the latent heat flux variation decomposition. The units of time series represent the product of specific humidity and wind speed.

latitudes higher than the Bering Strait, around 65°N, there is increased variability in the zonal wind direction in 2019 as measured by the saildrones.

The sea-air temperature differences in Figure 3 indicate that during these summer seasons, a significant proportion of stable and neutral AMBL conditions were observed, characterized by negative and near-zero values of temperature difference. During these periods, surface turbulent heat fluxes were often negative, corresponding to energy input into the ocean. Several studies have focused on estimating the transitional period during which the ocean shifts from absorbing heat to releasing it (Carrigg et al., 2024). Understanding how this period is influenced by physical factors is crucial for estimating long-term variations in Arctic warming.

Figures 4 and 5 decompose the temporal variation of sensible and latent heat fluxes into three subterms, which can be compared with the sea-air temperature differences shown in Figure 3. The decomposition method, detailed in Section 2.5, highlights the contributions of each subterm to the total heat flux variation. Note that the focus here is on comparing the relative contributions rather than the exact values of each term. Therefore, the units in these figures represent the product of temperature (or humidity) and wind speed.

Across all 5 years, the total variation in sensible heat flux is primarily driven by variations in the air-sea temperature difference, denoted as the *T*term in the figures. In contrast, temporal variations in wind speed, represented as the *W*term, contribute less than 20% to the total flux in the region. The covariance between wind and temperature, denoted as the *C*term, sometimes contributes equally to or even more significantly than the *W*term to the total heat flux. The *T*term has the lowest contribution of year 2020 compared to other years, accounting for approximately 66% of the total sensible heat flux variation. Conversely, in 2019 and 2022, the *T*term is the dominant factor explaining, respectively, 90% and 87% of the total variance.

The three flux components in Equation 5 underwent similar variability (Figure 5) as seen for the total flux (Figure 4). This comparison highlights the consistency in the dominant factors affecting both types of THF variations. For the years 2018, 2019, and 2021, the contribution of the *C*term to sensible heat flux variations is greater than that of the *W*term, whereas the reverse is observed for latent heat fluxes. This suggests that the variability of wind is relatively larger than that of the air-sea humidity difference in comparison to that of the air-sea temperature difference. The role of wind in determining THF will be further explored in the next subsection,

21699291, 2025, 7, Downloaded from https://agupubs.onlinelibrary.wiley.com/doi/10.1029/2024JC022313 by Mbl Whoi Library, Wiley Online Library on [30/06/2025]. See the Terms and Conditions (https://onlinelibrary.wiley.com/terms-and-conditions) on Wiley Online Library for rules of use; OA articles are governed by the applicable Creative Commons License

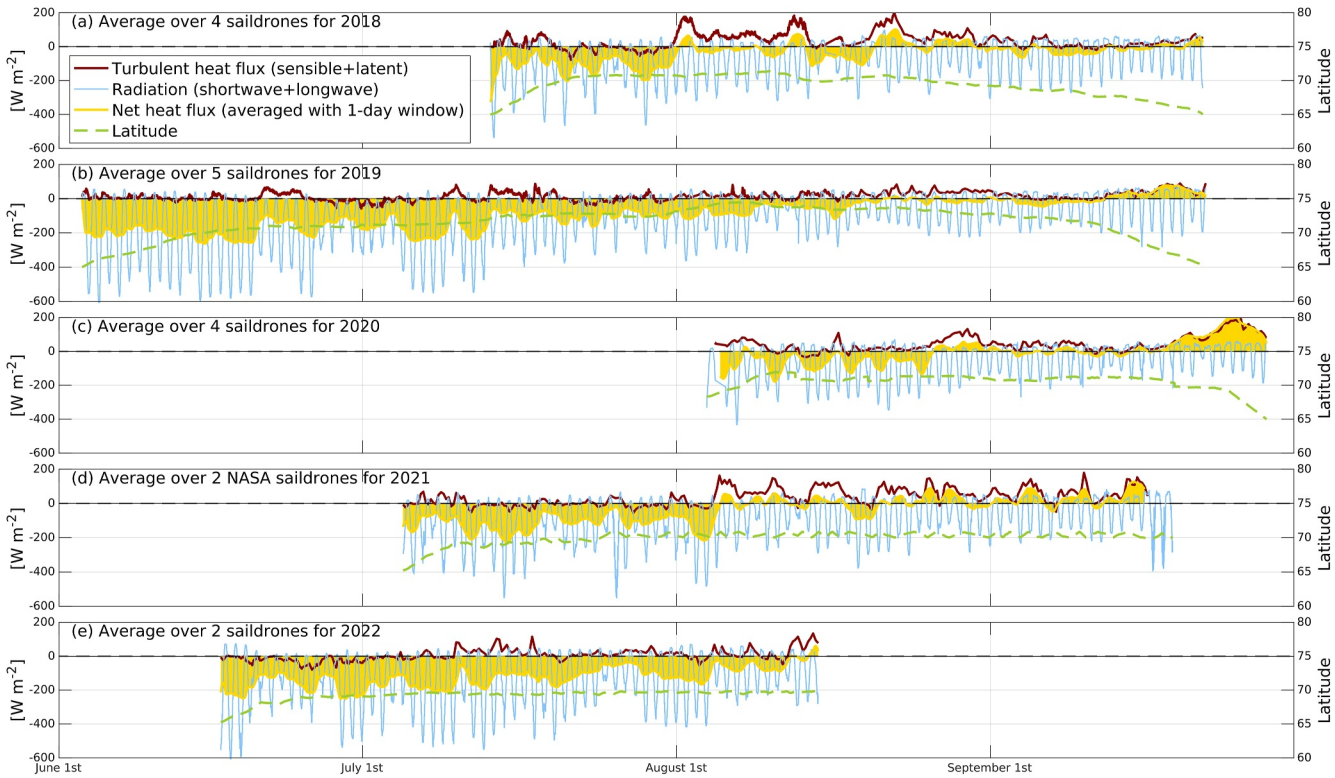

Figure 6. Time series of turbulent heat fluxes from saildrones, radiation (NASA CERES), and net heat fluxes from June to September for the years 2018–2022. The data are limited to latitudes higher than 65°N. The time series of latitude is also shown to indicate the approximate measurement locations, providing context for interpreting the observed fluxes in relation to the regional climate.

offering a deeper understanding of how wind variations might influence the overall turbulent heat exchange between the sea and the atmosphere.

The combined THF and radiation along the saildrone tracks (Figure 6) clearly depict both the diurnal and seasonal cycles of total radiation corresponding to Earth's rotation and its orbit around the Sun, respectively. The net heat flux is calculated as the sum of radiative and turbulent contributions, highlighting the transitional period from summer to autumn when outgoing turbulent heat fluxes surpass radiative heat gain. Accurate estimates of this transitional period depend on precise quantification of both radiative processes and turbulent heat fluxes. Although accurate cloudiness detection is crucial for estimating radiative processes, calculating and parameterizing THF presents a significant challenge. Many commonly used algorithms, such as the COARE algorithm (Edson et al., 2013; Fairall et al., 1997, 2003), do not explicitly account for the predominantly stable to neutral conditions of the AMBL in high-latitude summer, which complicates the accurate estimation of THF in these regions.

3.2. Modifications of AMBL Stability in Two Scenarios

To investigate the significance of wind in determining air-sea THF, we present examples of transitions in wind patterns for each year in Figure 7. These transitional periods and sea-air temperature difference were selected based on the maximum gradient in THF variation, as observed in the saildrone measurements shown in Figure 3. In the examples of 2018, 2019, and 2020, the data illustrate a transition where the ocean shifts from absorbing heat to releasing it. This transition is consistent with a change in the wind direction at the saildrone locations from northward to southward.

In contrast, the examples of the last two years (2021 and 2022) exhibit a different pattern, showing a transition from upward to downward air-sea THF. This shift aligns with changes in the spatial wind patterns, indicating that variations in wind direction and the associated thermal advection significantly influence the sign and magnitude

21699291, 2025, 7, Downloaded from https://agupubs.onlinelibrary.wiley.com/doi/10.1029/2024JC022313 by Mbl Whoi Library, Wiley Online Library on [30/06/2025]. See the Terms and Conditions (https://onlinelibrary.wiley.com/terms-and-conditions) on Wiley Online Library for rules of use; OA articles are governed by the applicable Creative Commons License

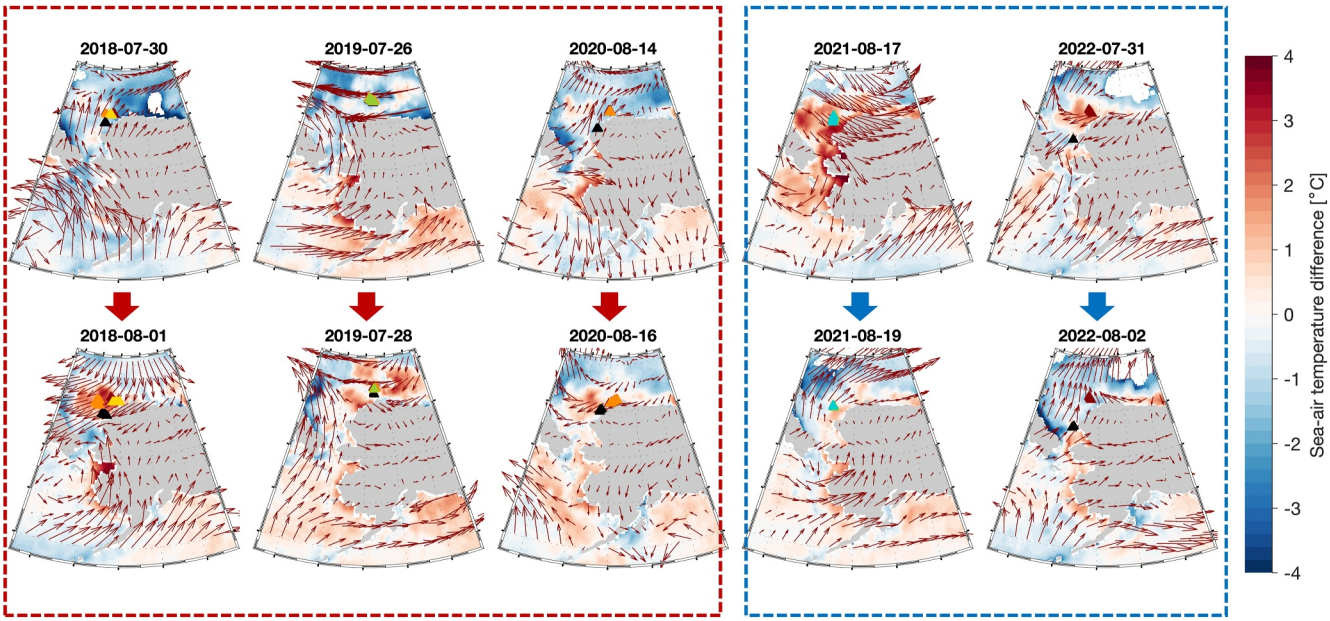

Figure 7. Some examples of synoptic changes in wind directions and sea-air temperature differences (colors) in the study area (ERA5). The saildrones' location is indicated by colored triangles in the map. The 2018, 2019, and 2020 examples show a transition from southerly to northerly that is associated with cold air outbreaks from higher latitudes. The 2021 and 2022 examples indicate a transition from northerly to southerly, connected with warm air advection coming from lower latitudes.

of THF during these periods. These cases underscore the critical role of synoptic-scale atmospheric variability in modulating air-sea interactions in the high-latitude environment.

We then consider 2020 and 2022 as two contrasting examples, with 2020 characterized by dominant northerly winds and 2022 by dominant southerly winds as shown in Figure 3. Figure 8 presents the frequency spectra of

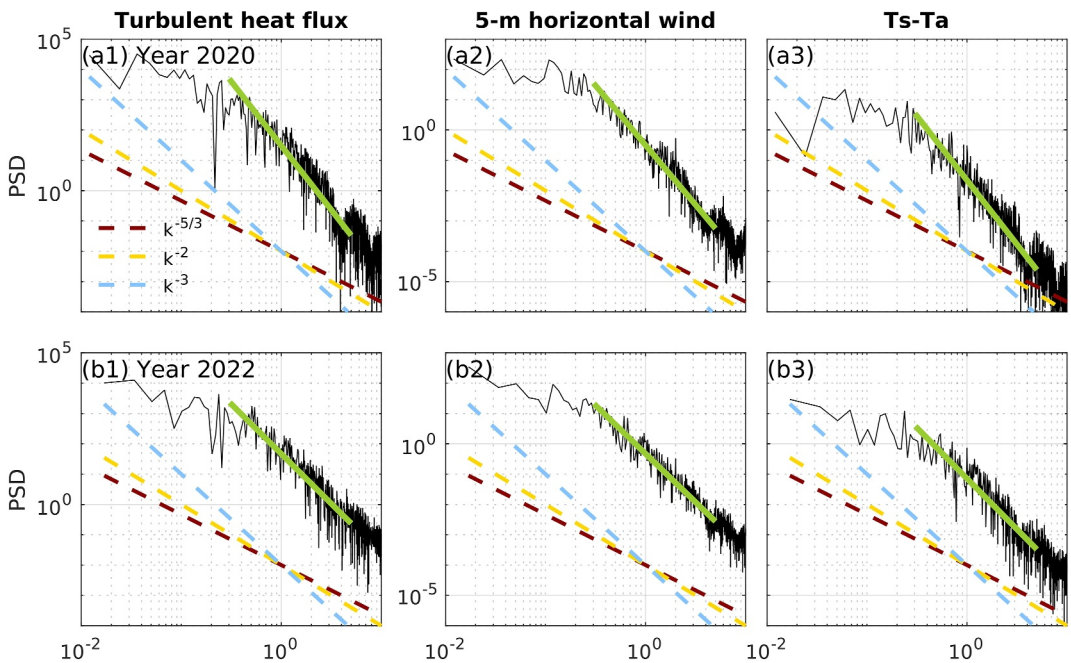

Figure 8. Frequency spectra for the years 2020 and 2022 for (a) turbulent heat fluxes (latent and sensible combined), (b) 5-m wind speed, and (c) sea-air temperature differences. PSD stands for Power Spectra Density. Note that the units vary by panel: (a1) and (b1) use $W^2\ m^{-4}\ s$, (a2) and (b2) use $m^2\ s^{-1}$, and (a3) and (b3) use $°C^2\ s$. The unit for frequency is s^{-1}.

21699291, 2025, 7, Downloaded from https://agupubs.onlinelibrary.wiley.com/doi/10.1029/2024JC022313 by Mbl Whoi Library, Wiley Online Library on [30/06/2025]. See the Terms and Conditions (https://onlinelibrary.wiley.com/terms-and-conditions) on Wiley Online Library for rules of use; OA articles are governed by the applicable Creative Commons License

Table 2
Slopes for the Frequency Spectra in the Log-Log Plot

Year	THF	Wind	Ts-Ta	Ts	Ta
2018	−2.8	−3.0	−2.8	−2.1	−3.0
2019	−2.3	−2.6	−2.2	−2.0	−2.7
2020	−4.2	−3.9	−4.2	−2.0	−3.3
2021	−3.6	−2.8	−3.6	−3.1	−2.8
2022	−3.3	−3.2	−3.4	−3.6	−3.7

Note. For each year, the entire time series was considered without any latitude restrictions.

THF, wind speed, and sea-air temperature difference for these 2 years. Before computing the frequency spectra, the original time series of each variable were interpolated to a consistent time step. Although the raw saildrone measurement interval is approximately 1 min, we interpolated the time series to a 14-min interval for the spectral analysis. Similarly, for the wavenumber spectra, each time series was first converted to a spatial domain based on the distance traveled by the saildrone, and then interpolated to uniform distance intervals.

The slopes of each spectrum in these log-log plots are summarized in Table 2 for all 5 years. Comparing 2020 and 2022, the slope of the THF spectrum is −4.2 for 2020, which is steeper than the −3.3 observed for 2022. This steep slope in THF for 2020 is also evident in the sea-air temperature difference and wind speed spectra. However, the slope for SST remains relatively mild, indicating that seawater temperature contains more comparable low- and high-frequency components. These factors suggest that in 2020, there was relatively constant wind direction from the north and a consistent air-sea temperature difference, despite higher variation in seawater temperature. This pattern indicates that the cold air advection in the Chukchi-Beaufort Sea region continually brought cold and dry air into the area, removing heat from the sea surface and destabilizing the AMBL.

Conversely, in 2022, the predominant southerly winds results in different dynamics, as reflected in the spectral slopes of the observed variables. Warm air advection stabilizes the marine boundary layer, producing a dual effect characterized by relatively similar but steep slopes in the frequency spectra of both air and seawater temperatures. Table 2 also shows that for the years 2018 and 2019, where warm air advection dominates (as shown in Figure 3), the slopes of THF remain relatively mild compared to 2022. However, the slopes of air temperature are steeper than those of water temperature for these 2 years, indicating that while the stabilizing effect does not affect the atmospheric boundary layer significantly, there is variation in the frequency components of seawater temperature induced by ocean dynamics.

These detailed comparisons between 2020 and 2022 highlight the different impacts of cold and warm air advection on the marine boundary layers. The analysis demonstrates that cold air advection can lead to consistent heat removal from the ocean surface layer and continuous destabilization of the AMBL. In contrast, warm air advection tends to stabilize the AMBL, resulting in more frequent and synchronized changes in air and seawater temperatures, as observed in 2022. This indicates that cold air advection is more constant in the Beaufort-Chukchi region, whereas warm air advection from lower latitudes occurs as synoptic events or sudden bursts. This pattern is also evident in Figure 2, which shows the general wind patterns from June to September, highlighting the predominant northeasterly wind, that is, cold air advection, during the summer months.

We further explore the spatial variations in Figure 9 for the years 2020 and 2022, each characterized by different boundary layer stability conditions. This figure presents the coupling coefficients between SST and THF as a function of the saildrones' travel distance. These SST-THF coupling coefficients are crucial for determining whether the atmosphere or ocean is the primary driver in air-sea interactions and for quantifying the sensitivity of turbulent heat fluxes to SST (Hausmann et al., 2017). The analysis uses three spatial windows, corresponding to scales larger than 10, 100, and 1,000 km. In the Arctic Ocean, the Rossby radius is approximately 10 km (Nurser & Bacon, 2014), which is significantly smaller than the typical ∼100 km scale in the subtropics, necessitating a reconsideration of scaling analyses when comparing these regions. The slopes in the log-log plots of Figure 9, with the x-axis representing spatial scales, align with those in the frequency spectra shown in Figure 8. The year 2020 displays a steeper slope compared to 2022, indicating more varied spatial scales in 2022, consistent with a stabilizing AMBL.

A summary of the mean, median, and maximum (or minimum) values of SST-THF coupling coefficients at these three scales is provided in Table 3. The mean value of the SST-THF coupling coefficient is about 10 W m^{-2} °C^{-1} for unstable conditions and −0.5 W m^{-2} °C^{-1} for stable conditions. However, the difference of maximal values of coupling coefficients between the stable year 2022 and unstable year 2020 is much further apart. The minimum value of −45 W m^{-2} °C^{-1} is comparable to the SST-THF coupling coefficient in midlatitude ocean frontal zones. In these frontal regions, the variability of air-sea heat fluxes is driven by SST variations arising from intrinsic

21699291, 2025, 7, Downloaded from https://agupubs.onlinelibrary.wiley.com/doi/10.1029/2024JC022313 by Mbl Whoi Library, Wiley Online Library on [30/06/2025]. See the Terms and Conditions (https://onlinelibrary.wiley.com/terms-and-conditions) on Wiley Online Library for rules of use; OA articles are governed by the applicable Creative Commons License

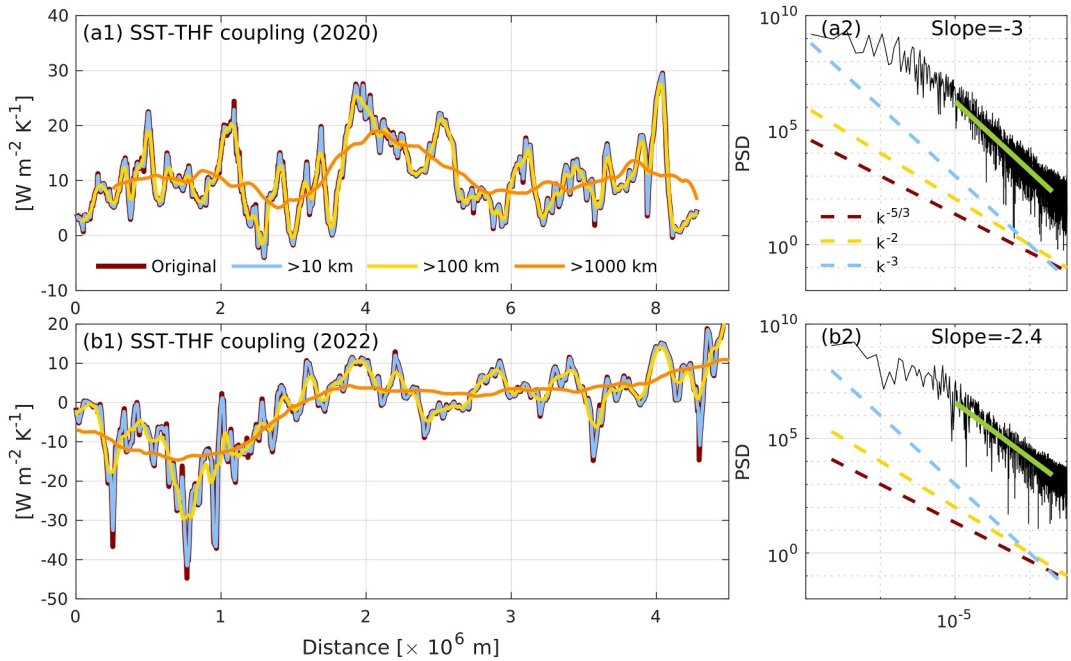

Figure 9. Air-sea coupling coefficients between sea surface temperature and turbulent heat flux (THF) for years 2020 and 2022. The right panels show wavenumber spectra of THF. PSD denotes power spectral density with units of $W^2\ m^{-3}$. The unit for wavenumber is m^{-1}.

oceanic variability rather than atmospheric variations (Small et al., 2019). Therefore, it remains interesting to quantify the different factors that determine air-sea THF variability at high latitudes.

3.3. Dependence of Air-Sea Heat Fluxes on AMBL Stability

This section further investigates the relationship between air-sea heat fluxes and different conditions of the AMBL. Figure 10 presents the histograms of THF, wind speed, air relative humidity, sea-air temperature difference, wind direction, and the Monin-Obukhov stability parameter ζ all based on the saildrone observations, separated into red and blue for higher and lower latitudes, with the latitude separation criterion at the Bering Strait of 65°N. The distribution comparison between higher-latitude THF and that of the lower-latitude reveals that near-zero THF is more commonly observed at higher latitudes. The median THF ranges from −10 to 10 W m^{-2} for higher latitudes and from 10 to 30 W m^{-2} for lower latitudes. The combination of wind speed (Figure 10b) and air humidity (Figure 10c) shows that higher latitudes are associated with lower wind speeds and saturated air, compared to lower latitudes (Andreas et al., 2002).

Table 3
Scale-Dependent SST-THF Coupling Coefficients for Years 2020 and 2022

	Original	≥10 km	≥100 km	≥1,000 km
Mean (2020)	10.50	10.51	10.55	10.85
Median (2020)	9.52	9.54	9.72	10.21
Extreme (2020)	29.54	29.41	27.54	19.02
Mean (2022)	−0.50	−0.50	−0.50	−0.66
Median (2022)	1.04	1.09	1.53	2.90
Extreme (2022)	−44.72	−41.57	−29.69	−14.61

Note. Units for the SST-THF coupling coefficients: W m^{-2} °C^{-1}.

The pattern for sea-air temperature differences between higher and lower latitudes in Figure 10d shows that lower latitudes exhibit larger positive values under unstable AMBL conditions. Figure 10e reveals comparable northward and southward components of the wind direction, with a higher proportion of northward winds observed at both latitude bands. At higher latitudes, westward winds are predominant in terms of zonal directions. The stability parameter in Figure 10f indicates that the AMBL is generally neutral in stability at both higher and lower latitudes, with a maximum value of ζ around 0.4, contributing to 2% of the total measurements.

These observations suggest significant differences in air-sea interaction dynamics between higher and lower latitudes (separated by 65°N). At higher latitudes, near-zero turbulent heat fluxes, lower wind speeds, and saturated air conditions indicate a more stable and less dynamic AMBL. In contrast, lower latitudes experience greater turbulent heat fluxes, stronger winds, and more

21699291, 2025, 7, Downloaded from https://agupubs.onlinelibrary.wiley.com/doi/10.1029/2024JC022313 by Mbl Whoi Library, Wiley Online Library on [30/06/2025]. See the Terms and Conditions (https://onlinelibrary.wiley.com/terms-and-conditions) on Wiley Online Library for rules of use; OA articles are governed by the applicable Creative Commons License

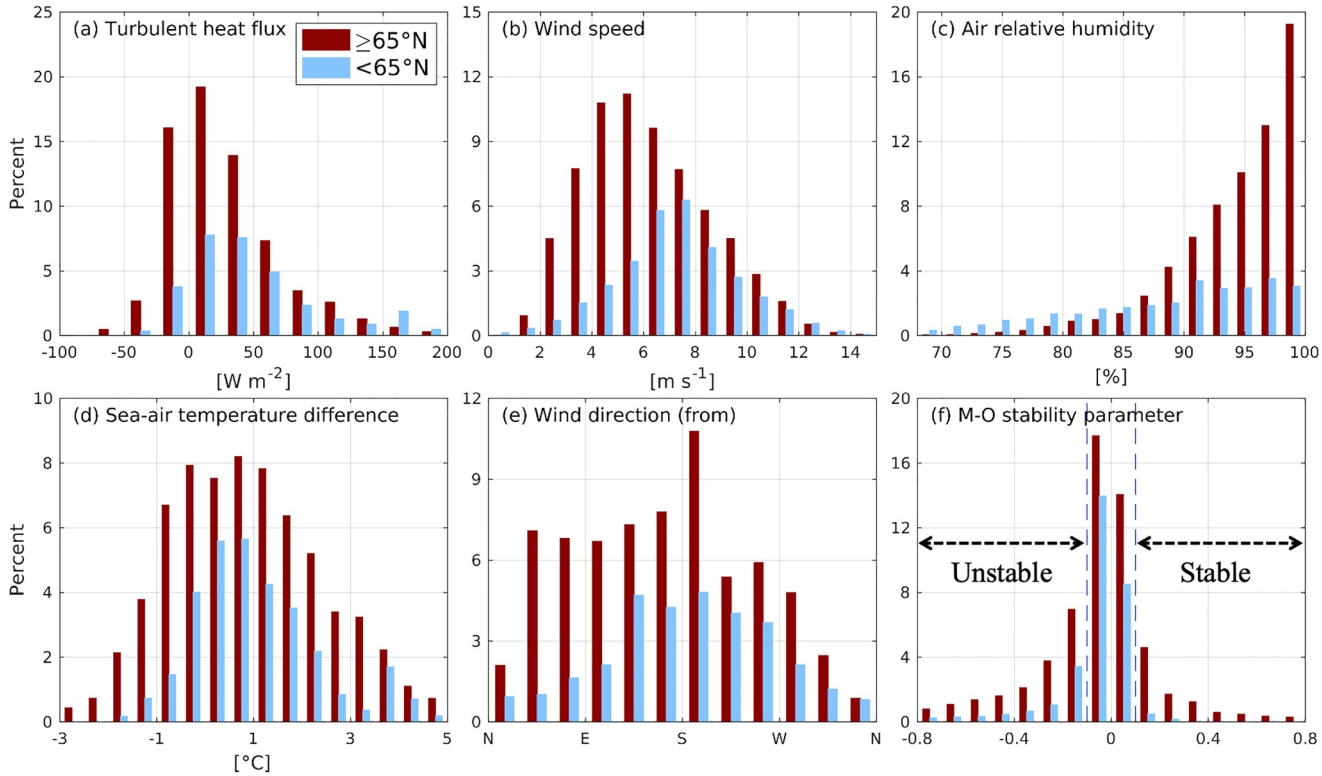

Figure 10. Histograms of sailrone measurements separated into latitudes higher (red) and lower (blue) than 65°N. (a) Turbulent heat flux, (b) wind speed, (c) air relative humidity, (d) sea-air temperature difference, (e) wind direction (from), and (f) Monin-Obukhov stability parameter ζ. Conditions of stability are defined in the text.

pronounced sea-air temperature differences, reflecting a more active and unstable AMBL.

Figure 11 explores the relationship between atmospheric variables and air-sea temperature difference or Monin-Obukhov stability, both used to define the AMBL stability. Figures 11a and 11c illustrate the regression of the Monin-Obukhov stability parameter ζ against the sea-air temperature difference, and vice versa. The distribution of the number of measurements indicates that stability based on sea-air temperature difference is more spread out, whereas the distribution based on ζ resembles a normal distribution and is more concentrated at neutrally stable conditions. The regression of ζ to sea-air temperature difference is linear within the range of -3 and 5°C. However, the regression of sea-air temperature difference to the Monin-Obukhov stability parameter is nonlinear.

As the AMBL becomes more unstable (with the definition of stability based on air-sea temperature difference), the wind direction tends to shift from a southerly to northerly, as shown in Figure 11b. This relationship between the wind direction and sea-air temperature difference is almost linear, although some uncertainties are observed when air and seawater temperatures are nearly indistinguishable. The lower panels of Figure 11 examine how wind speed, wind direction, and air relative humidity correlate with the Monin-Obukhov stability parameter. Since ζ accounts for both mechanical and thermodynamic contributions, it is not surprising to observe a normal distribution of wind speed as a function of ζ. This further indicates that at neutral AMBL conditions, defined by ζ, wind speeds reach their peak of approximately 9 m s^{-1}.

The wind direction shown in Figure 11e is more associated with stable AMBL conditions ($\zeta > 0$), where winds predominantly blow from the south. However, this relationship between wind direction and Monin-Obukhov stability is less pronounced than its relationship with sea-air temperature difference (Figure 11b). Similar to Figure 11b, anomalous wind directions are also observed under neutral AMBL conditions. Figure 11f suggests an almost linear relationship between relative humidity and the Monin-Obukhov stability parameter. This linear relationship underscores the importance of both mechanical and thermal factors in defining the stability of the AMBL. The linear and nonlinear relationships observed between ζ, sea-air temperature differences, wind direction, and relative humidity provide valuable insights into the behavior of the AMBL under various stability

21699291, 2025, 7, Downloaded from https://agupubs.onlinelibrary.wiley.com/doi/10.1029/2024JC022313 by Mbl Whoi Library, Wiley Online Library on [30/06/2025]. See the Terms and Conditions (https://onlinelibrary.wiley.com/terms-and-conditions) on Wiley Online Library for rules of use; OA articles are governed by the applicable Creative Commons License

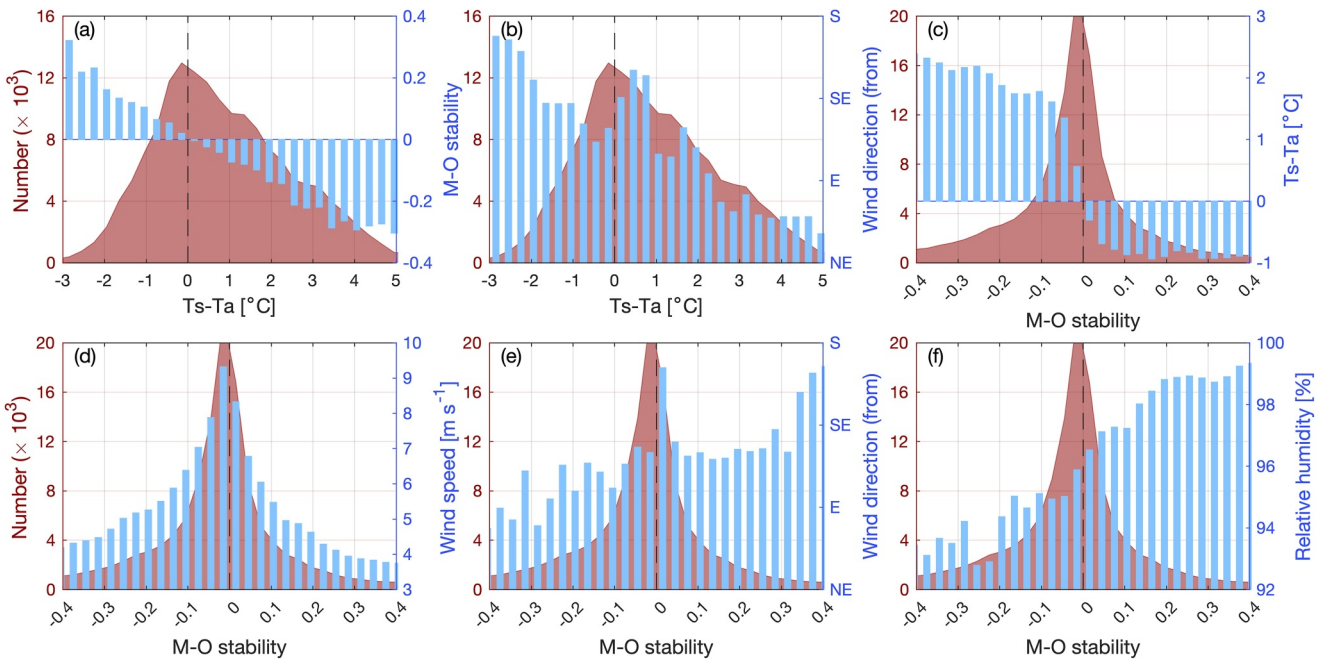

Figure 11. Sea-air temperature difference and Monin-Obukhov stability parameter ζ in defining atmospheric marine boundary layer stability. (a) Relationship between ζ and sea-air temperature difference; (b) wind direction as a function of sea-air temperature difference; (c) relationship between sea-air temperature difference and ζ; (d) wind speed as a function of ζ; (e) wind direction as a function of ζ (f) Air relative humidity as a function of ζ. Values in each bar represent medians.

conditions. This knowledge is essential for improving the parameterization of turbulent fluxes in climate models particularly in representing stability-dependent processes such as surface heat exchange, stratification, and cloud formation in high-latitude environments. Accurate representation of these processes is critical for simulating Arctic amplification and associated feedbacks.

As shown in Figures 10 and 11, we define AMBL stability conditions based on the Monin-Obukhov stability parameter ζ as follows: unstable conditions ($-0.6 \leq \zeta < -0.1$), neutral conditions ($-0.1 \leq \zeta < 0.1$), and stable conditions ($0.1 \leq \zeta < 0.6$). The cutoff criterion of 0.6 is not arbitrary; the density distribution in Figures 10f and 11 indicates that ζ values greater than 0.4 have negligible counts. As noted in the introduction, the definition of neutral conditions is based on empirical experiments, which is why we set the criterion at 0.1. Figure 11 demonstrates that this limit approximates one-third of the total measurements for neutral conditions.

To assess whether skin temperature measurements from NASA saildrone-borne radiometers can improve the accuracy of THF calculations under various AMBL stability conditions, we examine the correlation between several key variables and two definitions of AMBL stability: the Monin-Obukhov stability parameter and bulk-air temperature difference in Figure 12. First, the time series of the bulk-air temperature difference and wind vector show a strong correspondence, consistent with the observations summarized in Section 3.2, where southward (northward) air advection correlates with unstable (stable) conditions. Second, the Monin-Obukhov stability parameter sometimes exhibits spikes when wind direction suddenly shifts while the wind speed is close to zero. This behavior may reflect abrupt changes in thermal advection, suggesting that shifts in wind direction—when associated with contrasting air mass properties—can serve as useful indicators of near-surface stability transitions at high latitudes.

Additionally, the correlation between the bulk-skin temperature difference and the two stability definitions shown in Figure 12 indicates that in 2019, there were more occurrences of the cool skin effect, as also observed by Jia and Minnett (2023). In contrast, 2021 exhibited a linear relationship between the two, suggesting that the warm layer effect predominated during this year. In other words, there were few instances where the skin temperature was cooler than both the air and bulk temperatures for the year of 2021. Since wind speed also affects the Monin-Obukhov stability parameter ζ, the correlation between the bulk-skin temperature difference and ζ is nonlinear.

21699291, 2025, 7, Downloaded from https://agupubs.onlinelibrary.wiley.com/doi/10.1029/2024JC022313 by Mbl Whoi Library, Wiley Online Library on [30/06/2025]. See the Terms and Conditions (https://onlinelibrary.wiley.com/terms-and-conditions) on Wiley Online Library for rules of use; OA articles are governed by the applicable Creative Commons License

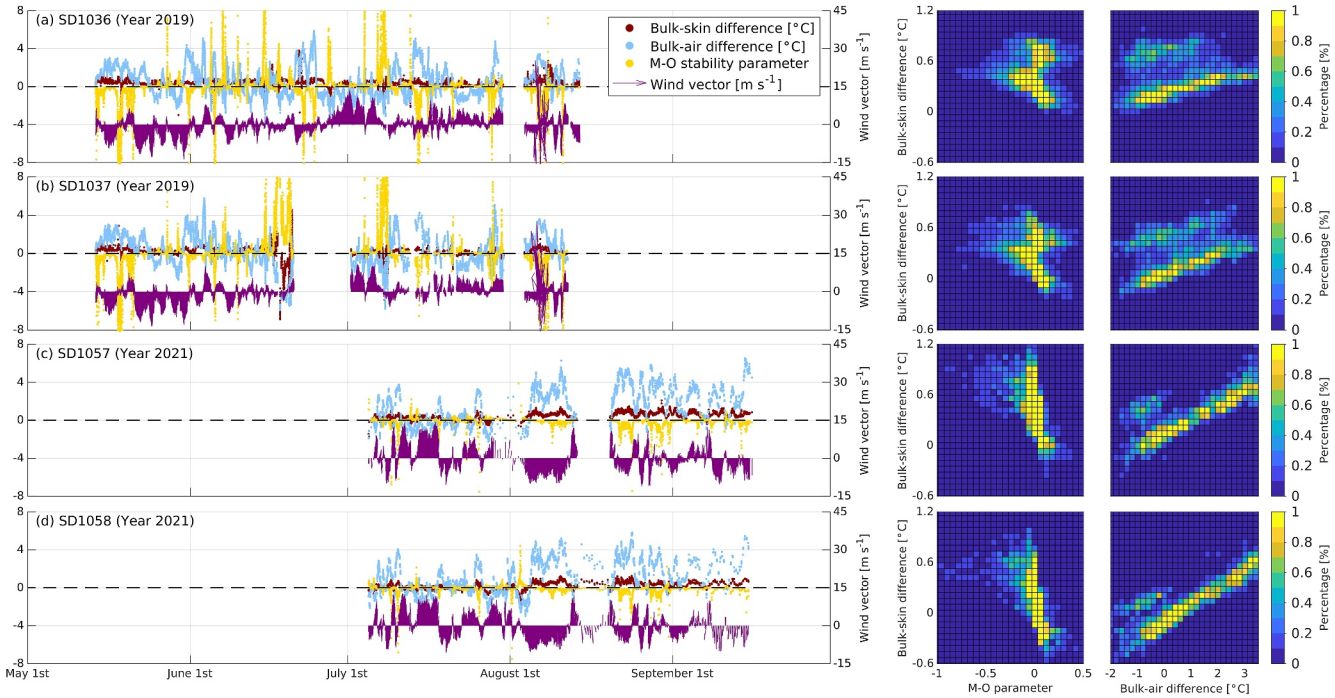

Figure 12. Left: Time series of the bulk-skin sea surface temperature (SST) difference, bulk-air temperature difference, Monin-Obukhov stability parameter, and wind vector are shown for four NASA saildrones that measured sea surface skin temperatures: (a) SD1036 and (b) SD1037 from 2019, and (c) SD1057 and (d) SD1058 from 2021. Right: Two density distributions as functions of the bulk-skin SST difference and the Monin-Obukhov stability parameter, and the bulk-skin SST difference and the bulk-air temperature difference, respectively representing the two methods used to define atmospheric marine boundary layer stability.

A linear regression can be established within the bulk-air temperature difference range of −2 to 4°C, as shown in both Figures 12 and 13a. As noted in Figure 12, the relationship between the bulk-skin temperature difference and the Monin- Obukhov stability parameter is nonlinear; however, a similar line has been added in Figure 13c to illustrate the three quadrants with most possible observations. Schematics related to (a) and (c) are shown in (b) and (d), respectively.

The combination of (a) and (b) in Figure 13 indicates that measurements often show a positive bulk-skin temperature difference (i.e., cool skin effect) in quadrants I and II across the four NASA saildrones. Conversely, the warm layer effect observed in quadrant III is less pronounced compared to the cool skin effect. Additionally, when using bulk-air temperature difference to define boundary layer stability, the measurements show a comparable number of stable and unstable conditions. The combination of (c) and (d) reverses the x-axis of (a) and (b) to reflect boundary layer stability. These panels show the correlation between the bulk-skin temperature difference and the Monin-Obukhov stability parameter. Thus, the three quadrants with the most measurements are I, II, and IV. Figure 13d also distinguishes different stability conditions along the x-axis: neutral stability is controlled by wind shear, whereas the left side represents buoyancy-driven mixing and the right side represents enhanced stratification.

To distinguish between the cool skin and warm layer effects in the surface skin layer, we list in Table 4 the percentage of measurements in each quadrant of Figure 13 for the years 2019 and 2021. Notably, quadrant II contains about 22% more measurements than quadrant III in 2019. This discrepancy supports the development of a new model by Jia and Minnett (2023), which primarily accounts for the cool skin effect while considering diurnal warming (i.e., warm layer effect) as a secondary factor for this region. However, with the new data from 2021, the warm layer effect now predominates over the cool skin effect, representing approximately 3% more measurements. This change is also evident in Figure 13c that shows the relationship between bulk-skin temperature difference and the Monin-Obukhov stability parameter: quadrant I is about 25% more prevalent than quadrant IV in 2019, whereas quadrant IV is 3% more prevalent than quadrant I in 2021.

21699291, 2025, 7, Downloaded from https://agupubs.onlinelibrary.wiley.com/doi/10.1029/2024JC022313 by Mbl Whoi Library, Wiley Online Library on [30/06/2025]. See the Terms and Conditions (https://onlinelibrary.wiley.com/terms-and-conditions) on Wiley Online Library for rules of use; OA articles are governed by the applicable Creative Commons License

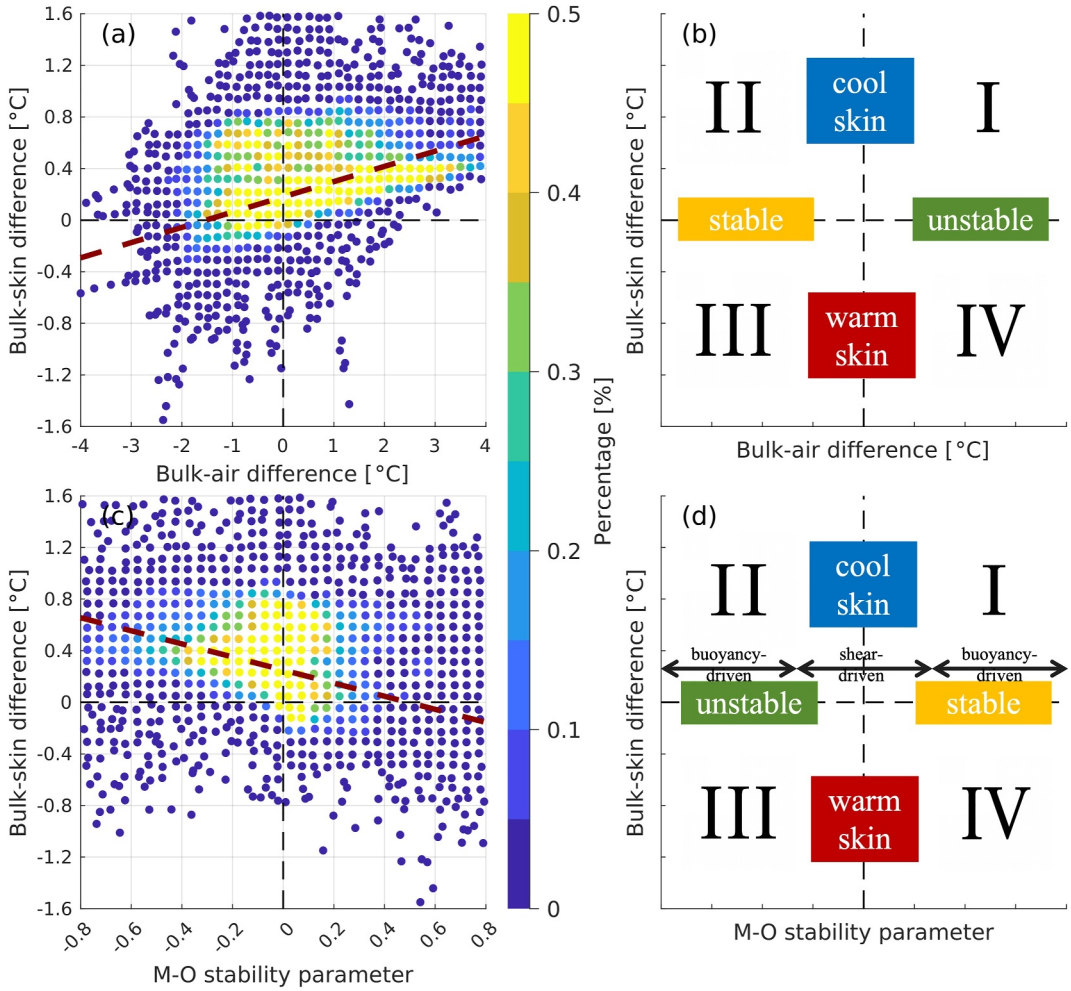

Figure 13. (a) Relationship between the bulk-skin temperature difference and the bulk-air temperature difference for four NASA saildrones. The colors represent the percentage of observations in each bin. (b) Schematic representation of the conditions shown in (a). (c) Relationship between the bulk-skin temperature difference and the Monin-Obukhov stability parameter ζ for four NASA saildrones. (d) Schematic representation of the conditions shown in (c).

We quantify the pure warm layer effect in the Arctic summer, specifically, to isolate the warm layer effect by removing instances where the skin temperature is higher than both the air and bulk temperatures. Figure 14 compares turbulent heat fluxes estimated with or without using skin temperatures by the COARE algorithm with three approaches: (a) seawater bulk temperature with cool skin correction applied, (b) seawater bulk temperature without cool skin correction, and (c) measured skin temperature without adjustments. Boundary layer stability was defined under three conditions by 2 methods: the Monin–Obukhov stability parameter ζ (introduced

Table 4
Percentage (%) of Measurements in Each Quadrant in Figure 13

	Quadrant I	Quadrant II	Quadrant III	Quadrant IV
Total (bulk-air difference)	57.3	31.9	9.6	1.3
Year 2019	57.2	32.6	9.2	1.1
Year 2021	59.9	15.5	18.4	6.3
Total (M-O stability parameter)	34.6	54.2	1.2	10.0
Year 2019	35.4	54.0	1.0	9.6
Year 2021	15.9	59.4	6.0	18.6

21699291, 2025, 7, Downloaded from https://agupubs.onlinelibrary.wiley.com/doi/10.1029/2024JC022313 by Mbl Whoi Library, Wiley Online Library on [30/06/2025]. See the Terms and Conditions (https://onlinelibrary.wiley.com/terms-and-conditions) on Wiley Online Library for rules of use; OA articles are governed by the applicable Creative Commons License

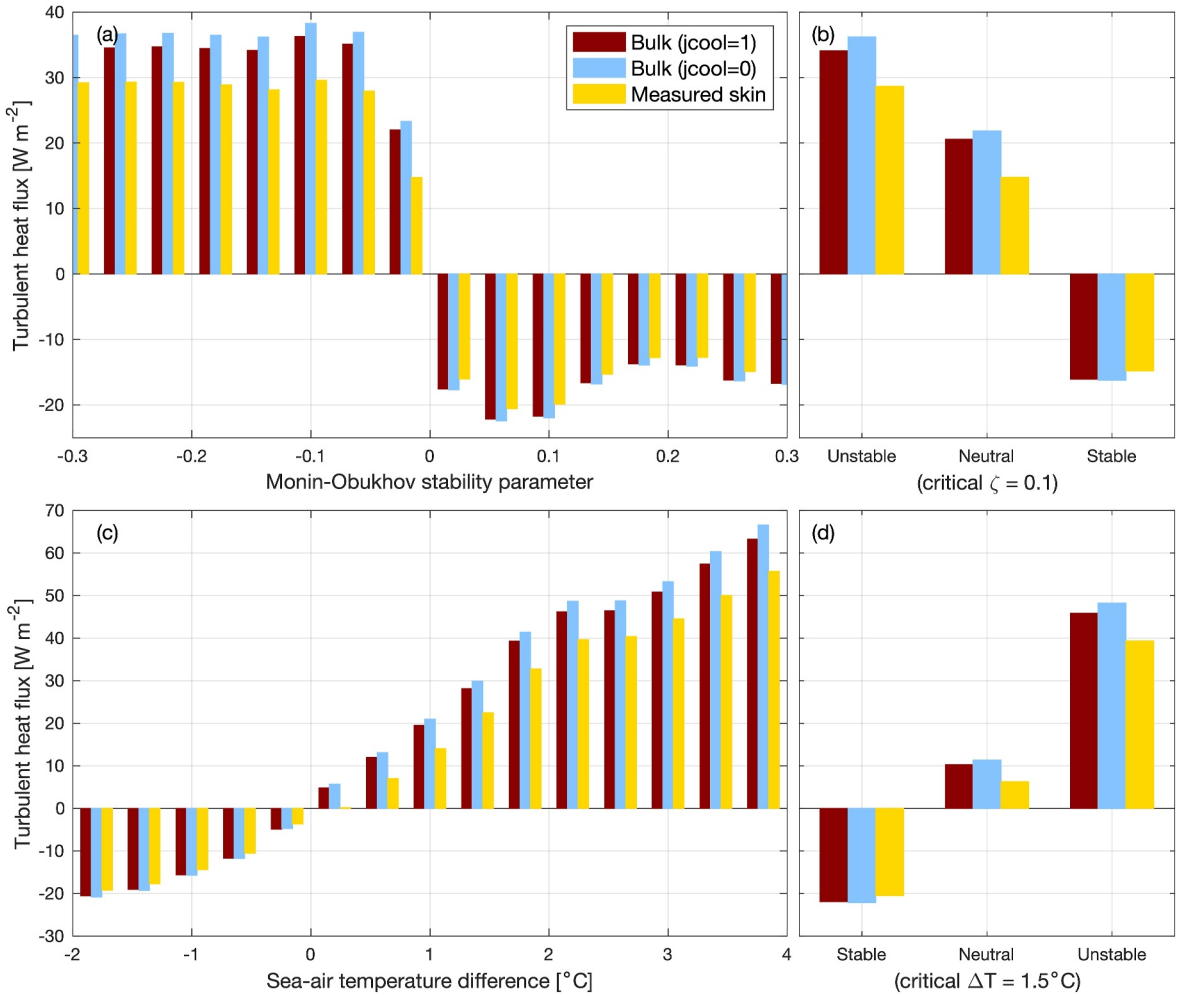

Figure 14. Turbulent heat fluxes as functions of (a) the Monin-Obukhov stability parameter ζ and (c) sea-air temperature difference ΔT. The figure compares three settings using the COARE algorithm: (1) seawater bulk temperature with cool skin correction, (2) seawater bulk temperature without cool skin correction, and (3) measured skin temperature without any corrections. Panels (a) and (c) illustrate the variation in heat fluxes across different stability parameter ranges. Panels (b) and (d) present the average heat flux values for each COARE algorithm setting under different stability conditions. Values in each bar represent the mean of the measurements.

previously) and a sea-air temperature difference-based classification, which defines stable conditions ($-4°C \leq \Delta T < -1.5°C$), neutral conditions ($-1.5°C \leq \Delta T < 1.5°C$), and unstable conditions ($1.5°C \leq \Delta T < 4°C$). To ensure the relevance of the temperature ranges and to eliminate outliers, we removed the bulk-air temperature differences greater than 5°C and bulk-skin temperature differences greater than 1°C.

For unstable conditions, as defined by the Monin–Obukhov stability parameter ($-0.6 \leq \zeta < -0.1$), the implementation of cool skin correction results in a reduction of outgoing THF by approximately 6% from that when seawater bulk temperature is used. In contrast, when using measured skin temperature, the reduction in THF is more pronounced, approximately 21%. This general trend persists under neutral conditions ($-0.1 \leq \zeta < 0.1$). Under stable conditions ($0.1 \leq \zeta < 0.6$), the application of cool skin correction increases the air-sea temperature difference, which in turn leads to an erroneous enhancement of downward THF into the ocean. However, when measured skin temperatures are used, the downward THF decreases by about 9%. This suggests that using measured skin temperatures rather than corrected bulk temperatures generally results in a reduced magnitude of THF, thereby modifying the air-sea heat budget in a significant manner. This highlights the importance of considering AMBL stability conditions when interpreting skin and bulk temperature relationships and their subsequent impact on THF calculations.

21699291, 2025, 7, Downloaded from https://agupubs.onlinelibrary.wiley.com/doi/10.1029/2024JC022313 by Mbl Whoi Library, Wiley Online Library on [30/06/2025]. See the Terms and Conditions (https://onlinelibrary.wiley.com/terms-and-conditions) on Wiley Online Library for rules of use; OA articles are governed by the applicable Creative Commons License

Table 5
Turbulent Heat Flux, Net Heat Flux, and SST-THF Coupling Coefficient in 3 Methods

	Unstable	Neutral	Stable
Turbulent heat flux			
Bulk (jcool = 1)	33.5	20.6	−15.2
Bulk (jcool = 0)	35.6	21.9	−15.3
Real skin (jcool = 0)	28.2	14.8	−13.9
Net heat flux			
Bulk (jcool = 1)	−112.5	−113.1	−126.9
Bulk (jcool = 0)	−110.4	−111.9	−127.1
Real skin (jcool = 0)	−117.7	−119.0	−125.7
SST-THF coupling coefficient			
Bulk (jcool = 1)	8.6	5.4	−3.6
Bulk (jcool = 0)	9.3	5.7	−3.7
Real skin (jcool = 0)	6.4	3.1	−3.6

Note. Stability conditions were separated based on Monin-Obukhov stability parameter ζ. Units for THF and net heat flux: W m^{-2}. Units for the SST-THF coupling coefficients: W m^{-2} °C^{-1}. The thresholds used to separate the data into different stability groups were chosen to ensure a similar number of measurements in each group. The standard deviations for each stability group are not significantly different, so this information has been omitted for clarity.

Table 5 summarizes turbulent heat fluxes, net heat fluxes, and the SST-THF coupling coefficients under different AMBL conditions using various representations of temperature in the COARE algorithm for calculating turbulent heat fluxes. The table only shows different stability conditions defined by ζ, as Figure 14 gives similar results in terms of the 2 methods of stability definition. The results of Table 5 show that utilizing real skin temperature measurements increases the downward net heat flux by 1.1 times under unstable and neutral conditions, while a decrease is observed under stable conditions.

Regarding the air-sea coupling coefficient, the use of real skin temperature measurements generally decreases the magnitude of the SST-THF coupling by 31%, 46%, and 3% for unstable, neutral, and stable conditions, respectively. These findings are consistent with expectations, as the use of real skin temperatures typically reduces the air-sea temperature difference, thereby lowering the THF. This highlights the importance of accurate skin temperature measurements in refining the estimates of air-sea heat fluxes and improving the understanding of air-sea interactions under varying stability conditions.

4. Conclusion and Discussion

This study provides an in-depth analysis of the AMBL in the Arctic region during the summer-to-autumn transition period utilizing a comprehensive data set collected by saildrones over five years from 2018 to 2022. The results emphasize the critical role of synoptic-scale events and surface conditions in modulating the AMBL stability, which in turn influences air-sea turbulent heat fluxes. Key findings from the study include:

1. Temporal Variability in THF: The analysis reveals significant temporal variations in sensible and latent heat fluxes. The dominant factor influencing the total sensible heat flux variation across the study period is the air-sea temperature difference, while wind speed and its covariance with temperature play secondary roles.
2. Impact of Wind Patterns: The wind direction significantly influences the transition between upward and downward turbulent heat fluxes. Northerly winds, associated with cold air advection, lead to a consistent removal of heat from the ocean surface, destabilizing the AMBL. In contrast, southerly winds bring warm air, stabilizing the AMBL and leading to more frequent and synchronized changes in air and seawater temperatures and suppressed turbulent heat exchanges.
3. Stability Conditions and Their Effects: This study identifies AMBL stability conditions using both the sea-air temperature difference and the Monin-Obukhov stability parameter ζ, with the latter serving as the primary definition because it better accounts for the balance between shear- and buoyancy-driven mixing patterns. Unstable conditions are characterized by higher sea-air temperature differences and more dynamic near-surface atmosphere, whereas stable conditions are associated with lower wind speeds and saturated air, leading to less dynamic structure.
4. Spatial Variability and Coupling Coefficients: The spatial analysis of SST-THF coupling coefficients highlights significant differences between unstable and stable AMBL conditions. Unstable years, such as 2020, show more consistent and larger heat flux variations, whereas stable years, like 2022, exhibit a wider range of coupling coefficients, indicating more varied spatial scales.
5. Sensitivity of Heat Flux Estimates: The accuracy of THF estimates is highly sensitive to the AMBL stability conditions. Algorithms not accounting for the predominant stable to neutral conditions in high latitudinal regions may significantly overestimate the magnitude of THF.

The findings of this study have important implications for understanding the evolving climate system in the Arctic region. The observed variations in AMBL stability and their impact on air-sea heat flux highlight the complex interplay between atmospheric and oceanic processes, particularly in the context of a warming Arctic. The results suggest the necessity for climate models to incorporate accurate representations of AMBL stability conditions. Traditional bulk flux algorithms, such as the COARE algorithm, may not adequately capture the unique thermal

21699291, 2025, 7, Downloaded from https://agupubs.onlinelibrary.wiley.com/doi/10.1029/2024JC022313 by Mbl Whoi Library, Wiley Online Library on [30/06/2025]. See the Terms and Conditions (https://onlinelibrary.wiley.com/terms-and-conditions) on Wiley Online Library for rules of use; OA articles are governed by the applicable Creative Commons License

features of high-latitude regions, leading to potential inaccuracies in predicting air-sea interactions and their contributions to the Arctic energy budget.

The significant influence of synoptic-scale events on AMBL stability and heat flux suggests that short-term atmospheric processes can have profound effects on the long-term climatic trends in the Arctic. Understanding these events and their frequency, particularly in the context of changing wind patterns and temperature gradients, is crucial for improving predictive capabilities. The use of saildrones in this study has proven invaluable for collecting high-resolution data in remote and harsh environments. These autonomous platforms provide continuous and detailed measurements that are essential for validating theoretical models and improving our understanding of air-sea interactions. Expanding the deployment of such platforms could enhance our ability to monitor and predict changes in the Arctic environment.

Future research should focus on further refining our understanding of AMBL stability mechanisms, especially under varying synoptic conditions. Additionally, it is crucial to explore the coupling between atmospheric stability and other oceanic processes, such as ice melt and ocean currents, to develop a more comprehensive view of the Arctic climate system. Our study has linked the maximal values of the Monin-Obukhov stability parameter ζ to sudden transitions in wind direction, suggesting that wind direction changes could be an important indicator of AMBL stability modification. Further empirical studies are needed to better compare the cool skin effect and warm layer effect in surface skin layers. This study primarily addresses the warm layer effect observed during the Arctic summer where a stable boundary layer results in a skin layer warmer than the in-depth seawater temperature but cooler than the overlying air temperature. Although the cool skin effect was noted, particularly in 2019, it was not analyzed in detail. In conclusion, this study highlights the critical need for accurate representation of AMBL stability in climate models and emphasizes the value of high-resolution observational data in enhancing our understanding of air-sea interactions in the rapidly changing Arctic region. By improving our knowledge of these processes, we can better predict the impacts of Arctic amplification on global climate dynamics.

Data Availability Statement

The saildrone data for the five-year period (2018–2022) were accessed from the NOAA PMEL ERDDAP website by selecting the respective years at https://data.pmel.noaa.gov/pmel/erddap/tabledap/. Specifically, the 2018 data are available at https://data.pmel.noaa.gov/pmel/erddap/tabledap/saildrone_arctic_2018.html, and the 2020 data at https://data.pmel.noaa.gov/pmel/erddap/tabledap/2020_arctic_nos_all.html. For 2019 and 2021, saildrone data sets must be selected individually on the ERDDAP site. NASA saildrone data were publicly accessible via https://search.earthdata.nasa.gov/search?q=saildrone%20arctic. The ERA5 reanalysis data were retrieved from the ECMWF Climate Data Store (Hersbach et al., 2020). Radiation data were obtained from the CERES website at https://ceres-tool.larc.nasa.gov/ord-tool/jsp/SYN1degEd41Selection.jsp. The PMEL contribution number is 5674.

Acknowledgments
We gratefully acknowledge the supports from NOAA Climate Program Office COM program Grant NA20OAR4310370 and NOAA Ocean Monitoring and Observing (GOMO) program Grant NA19OAR4320074.

References

Andreas, E. L., Guest, P. S., Persson, P. O. G., Fairall, C. W., Horst, T. W., Moritz, R. E., & Semmer, S. R. (2002). Near-surface water vapor over polar sea ice is always near ice saturation. *Journal of Geophysical Research*, *107*(C10), SHE8-1–SHE8-15. https://doi.org/10.1029/2000JC000411

Atlas, D., Walter, B., Chou, S.-H., & Sheu, P. J. (1986). The structure of the unstable marine boundary layer viewed by lidar and aircraft observations. *Journal of the Atmospheric Sciences*, *43*(13), 1301–1318. https://doi.org/10.1175/1520-0469(1986)043⟨1301:TSOTUM⟩2.0.CO;2

Berström, H., & Smedman, A.-S. (1995). Stably stratified flow in a marine atmospheric surface layer. *Boundary-Layer Meteorology*, *72*(3), 239–265. https://doi.org/10.1007/BF00836335

Betts, A. K., & Boers, R. (1990). A cloudiness transition in a marine boundary layer. *Journal of the Atmospheric Sciences*, *47*(12), 1480–1497. https://doi.org/10.1175/1520-0469(1990)047⟨1480:ACTIAM⟩2.0.CO;2

Bonino, G., Iovino, D., Brodeau, L., & Masina, S. (2022). The bulk parameterizations of turbulent air-sea fluxes in nemo4: The origin of sea surface temperature differences in a global model study. *Geoscientific Model Development*, *15*(17), 6873–6889. https://doi.org/10.5194/gmd-15-6873-2022

Brooks, I. M., Söderberg, S., & Tjernström, M. (2003). The turbulence structure of the stable atmospheric boundary layer around a coastal headland: Aircraft observations and modelling results. *Boundary-Layer Meteorology*, *107*(3), 531–559. https://doi.org/10.1023/A:1022822306571

Carrigg, J., Yu, L., Menezes, V. V., & Chen, Y. (2024). Autumnal equinox shift in arctic surface energy budget: Beaufort–Chukchi seas case study. *Journal of Geophysical Research: Oceans*, *129*(5), e2023JC020788. https://doi.org/10.1029/2023JC020788

Chelton, D. B., & Xie, S.-P. (2010). Coupled ocean-atmosphere interaction at oceanic mesoscales. *Oceanography*, *23*(4), 52–69. https://doi.org/10.5670/oceanog.2010.05

Cohen, J., Francis, J. A., & Pfeiffer, K. (2024). Anomalous arctic warming linked with severe winter weather in northern hemisphere continents. *Communications Earth and Environment*, *5*(1), 557. https://doi.org/10.1038/s43247-024-01720-0

21699291, 2025, 7, Downloaded from https://agupubs.onlinelibrary.wiley.com/doi/10.1029/2024JC022313 by Mbl Whoi Library, Wiley Online Library on [30/06/2025]. See the Terms and Conditions (https://onlinelibrary.wiley.com/terms-and-conditions) on Wiley Online Library for rules of use; OA articles are governed by the applicable Creative Commons License

Cronin, M. F., Gentemann, C. L., Edson, J., Ueki, I., Bourassa, M., Brown, S., et al. (2019). Air–sea fluxes with a focus on heat and momentum. *Frontiers in Marine Science*, *6*. https://doi.org/10.3389/fmars.2019.00430

Doelling, D. R., Sun, M., Nguyen, L. T., Nordeen, M. L., Haney, C. O., Keyes, D. F., & Mlynczak, P. E. (2016). Advances in geostationary-derived longwave fluxes for the ceres synoptic (syn1deg) product. *Journal of Atmospheric and Oceanic Technology*, *33*(3), 503–521. https://doi.org/10.1175/JTECH-D-15-0147.1

Donlon, C. J., Minnett, P. J., Gentemann, C., Nightingale, T. J., Barton, I. J., Ward, B., & Murray, M. J. (2002). Toward improved validation of satellite sea surface skin temperature measurements for climate research. *Journal of Climate*, *15*(4), 353–369. https://doi.org/10.1175/1520-0442(2002)015⟨0353:TIVOSS⟩2.0.CO;2

Edson, J. B., Hinton, A. A., Prada, K. E., Hare, J. E., & Fairall, C. W. (1998). Direct covariance flux estimates from mobile platforms at sea. *Journal of Atmospheric and Oceanic Technology*, *15*(2), 547–562. https://doi.org/10.1175/1520-0426(1998)015⟨0547:DCFEFM⟩2.0.CO;2

Edson, J. B., Jampana, V., Weller, R. A., Bigorre, S. P., Plueddemann, A. J., Fairall, C. W., et al. (2013). On the exchange of momentum over the open ocean. *Journal of Physical Oceanography*, *43*(8), 1589–1610. https://doi.org/10.1175/JPO-D-12-0173.1

Fairall, C. W., Bradley, E. F., Godfrey, J. S., Wick, G. A., Edson, J. B., & Young, G. S. (1996). Cool-skin and warm-layer effects on sea surface temperature. *Journal of Geophysical Research*, *101*(C1), 1295–1308. https://doi.org/10.1029/95JC03190

Fairall, C. W., Bradley, E. F., Hare, J. E., Grachev, A. A., & Edson, J. B. (2003). Bulk parameterization of air-sea fluxes: Updates and verification for the coare algorithm. *Journal of Climate*, *16*(4), 571–591. https://doi.org/10.1175/1520-0442(2003)016⟨0571:BPOASF⟩2.0.CO;2

Fairall, C. W., White, A. B., Edson, J. B., & Hare, J. E. (1997). Integrated shipboard measurements of the marine boundary layer. *Journal of Atmospheric and Oceanic Technology*, *14*(3), 338–359. https://doi.org/10.1175/1520-0426(1997)014⟨0338:ISMOTM⟩2.0.CO;2

Grachev, A. A., & Fairall, C. W. (1997). Dependence of the Monin–Obukhov stability parameter on the bulk richardson number over the ocean. *Journal of Applied Meteorology*, *36*(4), 406–414. https://doi.org/10.1175/1520-0450(1997)036⟨0406:DOTMOS⟩2.0.CO;2

Hausmann, U., Czaja, A., & Marshall, J. (2017). Mechanisms controlling the SST air–sea heat flux feedback and its dependence on spatial scale. *Climate Dynamics*, *48*(3), 1297–1307. https://doi.org/10.1007/s00382-016-3142-3

Hersbach, H., Bell, B., Berrisford, P., Hirahara, S., Horányi, A., Muñoz-Sabater, J., et al. (2020). The ERA5 global reanalysis. *Quarterly Journal of the Royal Meteorological Society*, *146*(730), 1999–2049. https://doi.org/10.1002/qj.3803

Jia, C., & Minnett, P. J. (2023). Ocean warm skin signals observed by saildrone at high latitudes. *Geophysical Research Letters*, *50*(7), e2022GL102384. https://doi.org/10.1029/2022GL102384

Jia, C., Minnett, P. J., & Luo, B. (2023). Significant diurnal warming events observed by saildrone at high latitudes. *Journal of Geophysical Research: Oceans*, *128*(1), e2022JC019368. https://doi.org/10.1029/2022JC019368

Jozef, G., Cassano, J. J., Solomon, A., Intrieri, J., & de Boer, G. (2024). Evaluation of the coupled arctic forecast system's representation of the arctic atmospheric boundary layer vertical structure during mosaic. *Elementa: Science of the Anthropocene*, *12*(1), 00136. https://doi.org/10.1525/elementa.2023.00136

Kara, A. B., Rochford, P. A., & Hurlburt, H. E. (2000). Efficient and accurate bulk parameterizations of air–sea fluxes for use in general circulation models. *Journal of Atmospheric and Oceanic Technology*, *17*(10), 1421–1438. https://doi.org/10.1175/1520-0426(2000)017⟨1421:EAABPO⟩2.0.CO;2

Kondo, J. (1975). Air-sea bulk transfer coefficients in diabatic conditions. *Boundary-Layer Meteorology*, *9*(1), 91–112. https://doi.org/10.1007/BF00232256

Large, W. G., McWilliams, J. C., & Doney, S. C. (1994). Oceanic vertical mixing: A review and a model with a nonlocal boundary layer parameterization. *Reviews of Geophysics*, *32*(4), 363–403. https://doi.org/10.1029/94RG01872

Luo, B., Minnett, P. J., Szczodrak, M., & Akella, S. (2022). Regional and seasonal variability of the oceanic thermal skin effect. *Journal of Geophysical Research: Oceans*, *127*(5), e2022JC018465. https://doi.org/10.1029/2022JC018465

Ma, R., & Mahesh, K. (2023). Boundary layer transition due to distributed roughness: Effect of roughness spacing. *Journal of Fluid Mechanics*, *977*, A27. https://doi.org/10.1017/jfm.2023.937

McPhaden, M. J., & Hayes, S. P. (1991). On the variability of winds, sea surface temperature, and surface layer heat content in the western equatorial pacific. *Journal of Geophysical Research*, *96*(S01), 3331–3342. https://doi.org/10.1029/90JC01726

Meinig, C., Burger, E. F., Cohen, N., Cokelet, E. D., Cronin, M. F., Cross, J. N., et al. (2019). Public–private partnerships to advance regional ocean-observing capabilities: A saildrone and NOAA-PMEL case study and future considerations to expand to global scale observing. *Frontiers in Marine Science*, *6*. https://doi.org/10.3389/fmars.2019.00448

Monin, A. S., & Obukhov, A. M. (1954). Basic laws of turbulent mixing in the ground layer of the atmosphere. *Trudy–Geologicheskiy Institut, Akademiya Nauk SSSR*, *151*, 163–187.

Nurser, A. J. G., & Bacon, S. (2014). The Rossby radius in the Arctic ocean. *Ocean Science*, *10*(6), 967–975. https://doi.org/10.5194/os-10-967-2014

Obukhov, A. M. (1971). Turbulence in an atmosphere with a non-uniform temperature. *Boundary-Layer Meteorology*, *2*(1), 7–29. https://doi.org/10.1007/BF00718085

Peng, S., Yang, Q., Shupe, M. D., Xi, X., Han, B., Chen, D., et al. (2023). The characteristics of atmospheric boundary layer height over the arctic ocean during mosaic. *Atmospheric Chemistry and Physics*, *23*(15), 8683–8703. https://doi.org/10.5194/acp-23-8683-2023

Persson, P. O. G. (2012). Onset and end of the summer melt season over sea ice: Thermal structure and surface energy perspective from Sheba. *Climate Dynamics*, *39*(6), 1349–1371. https://doi.org/10.1007/s00382-011-1196-9

Persson, P. O. G., Fairall, C. W., Andreas, E. L., Guest, P. S., & Perovich, D. K. (2002). Measurements near the atmospheric surface flux group tower at Sheba: Near-surface conditions and surface energy budget. *Journal of Geophysical Research*, *107*(C10), SHE21-1–SHE21-35. https://doi.org/10.1029/2000JC000705

Proshutinsky, A., Krishfield, R., Timmermans, M.-L., Toole, J., Carmack, E., McLaughlin, F., et al. (2009). Beaufort gyre freshwater reservoir: State and variability from observations. *Journal of Geophysical Research*, *114*(C1), C00A10. https://doi.org/10.1029/2008JC005104

Reeves Eyre, J. E. J., Cronin, M. F., Zhang, D., Thompson, E. J., Fairall, C. W., & Edson, J. B. (2023). Saildrone direct covariance wind stress in various wind and current regimes of the tropical pacific. *Journal of Atmospheric and Oceanic Technology*, *40*(4), 503–517. https://doi.org/10.1175/JTECH-D-22-0077.1

Renault, L., Masson, S., Oerder, V., Colas, F., & McWilliams, J. C. (2023). Modulation of the oceanic mesoscale activity by the mesoscale thermal feedback to the atmosphere. *Journal of Physical Oceanography*, *53*(7), 1651–1667. https://doi.org/10.1175/JPO-D-22-0256.1

Rogers, D. P., Johnson, D. W., & Friehe, C. A. (1995). The stable internal boundary layer over a coastal sea. Part I: Airborne measurements of the mean and turbulence structure. *Journal of the Atmospheric Sciences*, *52*(6), 667–683. https://doi.org/10.1175/1520-0469(1995)052⟨0667:TSIBLO⟩2.0.CO;2

Saunders, P. M. (1967). The temperature at the ocean-air interface. *Journal of the Atmospheric Sciences*, *24*(3), 269–273. https://doi.org/10.1175/1520-0469(1967)024⟨0269:TTATOA⟩2.0.CO;2

21699291, 2025, 7, Downloaded from https://agupubs.onlinelibrary.wiley.com/doi/10.1029/2024JC022313 by Mbl Whoi Library, Wiley Online Library on [30/06/2025]. See the Terms and Conditions (https://onlinelibrary.wiley.com/terms-and-conditions) on Wiley Online Library for rules of use; OA articles are governed by the applicable Creative Commons License

Sauvage, C., Seo, H., Clayson, C. A., & Edson, J. B. (2023). Improving wave-based air–sea momentum flux parameterization in mixed seas. *Journal of Geophysical Research: Oceans*, *128*(3), e2022JC019277. https://doi.org/10.1029/2022JC019277

Seo, H., & Yang, J. (2013). Dynamical response of the arctic atmospheric boundary layer process to uncertainties in sea-ice concentration. *Journal of Geophysical Research: Atmospheres*, *118*(22), 12383–12402. https://doi.org/10.1002/2013JD020312

Serreze, M. C., & Barry, R. G. (2011). Processes and impacts of arctic amplification: A research synthesis. *Global and Planetary Change*, *77*(1), 85–96. https://doi.org/10.1016/j.gloplacha.2011.03.004

Small, R. J., Bryan, F. O., Bishop, S. P., & Tomas, R. A. (2019). Air–sea turbulent heat fluxes in climate models and observational analyses: What drives their variability? *Journal of Climate*, *32*(8), 2397–2421. https://doi.org/10.1175/JCLI-D-18-0576.1

Smedman, A.-S., Bergström, H., & Grisogono, B. (1997). Evolution of stable internal boundary layers over a cold sea. *Journal of Geophysical Research*, *102*(C1), 1091–1099. https://doi.org/10.1029/96JC02782

Sorbjan, Z., & Grachev, A. A. (2010). An evaluation of the flux–gradient relationship in the stable boundary layer. *Boundary-Layer Meteorology*, *135*(3), 385–405. https://doi.org/10.1007/s10546-010-9482-3

Tjernström, M., Birch, C. E., Brooks, I. M., Shupe, M. D., Persson, P. O. G., Sedlar, J., et al. (2012). Meteorological conditions in the central arctic summer during the arctic summer cloud ocean study (ascos). *Atmospheric Chemistry and Physics*, *12*(15), 6863–6889. https://doi.org/10.5194/acp-12-6863-2012

Tjernström, M., & Graversen, R. G. (2009). The vertical structure of the lower arctic troposphere analyzed from observations and the era-40 reanalysis. *Quarterly Journal of the Royal Meteorological Society*, *135*(639), 431–443. https://doi.org/10.1002/qj.380

Uttal, T., Curry, J. A., McPhee, M. G., Perovich, D. K., Moritz, R. E., Maslanik, J. A., et al. (2002). Surface heat budget of the Arctic ocean. *Bulletin of the American Meteorological Society*, *83*(2), 255–276. https://doi.org/10.1175/1520-0477(2002)083⟨0255:SHBOTA⟩2.3.CO;2

Van Roekel, L., Adcroft, A. J., Danabasoglu, G., Griffies, S. M., Kauffman, B., Large, W., et al. (2018). The KPP boundary layer scheme for the ocean: Revisiting its formulation and benchmarking one-dimensional simulations relative to les. *Journal of Advances in Modeling Earth Systems*, *10*(11), 2647–2685. https://doi.org/10.1029/2018MS001336

Vihma, T. (2014). Effects of arctic sea ice decline on weather and climate: A review. *Surveys in Geophysics*, *35*(5), 1175–1214. https://doi.org/10.1007/s10712-014-9284-0

Woodgate, R. A. (2018). Increases in the pacific inflow to the arctic from 1990 to 2015, and insights into seasonal trends and driving mechanisms from year-round Bering strait mooring data. *Progress in Oceanography*, *160*, 124–154. https://doi.org/10.1016/j.pocean.2017.12.007

Yu, L. (2019). Global air–sea fluxes of heat, fresh water, and momentum: Energy budget closure and unanswered questions. *Annual Review of Marine Science*, *11*(1), 227–248. https://doi.org/10.1146/annurev-marine-010816-060704

Yu, L., Chen, Y., Gonzalez, A. O., Zhang, C., & Foltz, G. R. (2023). Dry air outbreak and significant surface turbulent heat loss during hurricane Ian: Satellite and saildrone observations. *Geophysical Research Letters*, *50*(23), e2023GL105583. https://doi.org/10.1029/2023GL105583

Zhang, D., Cronin, M. F., Meinig, C., Farrar, J. T., Jenkins, R., Peacock, D., et al. (2019). Comparing air–sea flux measurements from a new unmanned surface vehicle and proven platforms during the spurs-2 field campaign. *Oceanography*, *32*(2), 122–133. https://doi.org/10.5670/oceanog.2019.220

Zheng, Z., Harcourt, R. R., & D'Asaro, E. A. (2021). Evaluating Monin–Obukhov scaling in the unstable oceanic surface layer. *Journal of Physical Oceanography*, *51*(3), 911–930. https://doi.org/10.1175/JPO-D-20-0201.1

21699291, 2025, 7, Downloaded from https://agupubs.onlinelibrary.wiley.com/doi/10.1029/2024JC022313 by Mbl Whoi Library, Wiley Online Library on [30/06/2025]. See the Terms and Conditions (https://onlinelibrary.wiley.com/terms-and-conditions) on Wiley Online Library for rules of use; OA articles are governed by the applicable Creative Commons License